

## S1. Detailed procedure for CRI retrieval from the optical-iterative method

Starting from the measurement datasets, the following procedure was applied:

- The  $\beta_{\text{sca,no-tc}}(\lambda, \theta_1 - \theta_2)$  (non truncation-corrected scattering coefficient) was extrapolated at the seven  $\beta_{\text{abs}}$  wavelengths (370, 470, 520, 590, 660, 880, 950) using the SAE following Eq. (2) and Eq. (3);
- The SMPS aerosol number size distribution ( $dN(D_m)/d\log D_m$ ) was converted into  $dN(D_g)/d\log D_g$  assuming spherical particles ( $\chi=1$ ). For the SIRTa site the size distribution data within the 8.9-829 nm range was extrapolated with a cubic spline on a constant  $d\log=1/64$  to match the resolution of the PRG and RambForest size measurements. The extrapolated size was normalised to conserve the total number of particles ( $N_{\text{tot}}$ );
- The  $\beta_{\text{abs}}$  was corrected for multiple-scattering ( $C_{\text{ref}}$ ) using the  $C_{\text{ref}}=2.45$  following the ACTRIS recommendation
- Iteration on  $n$  in the  $[1.2, 2.0]$  range and a  $dn=0.01$  resolution and on  $k$  in  $[0, 0.02]$  range and a  $dk=0.001$ , in order to model the no truncation-corrected scattering and absorption coefficients ( $\beta_{\text{sca,no-tc}}(\lambda, \theta_1 - \theta_2), \beta_{\text{abs}}$ ) through a Mie code for homogenous spherical particles.

Minimisation of the root mean squared difference (RMSD) between observed and modelled  $\beta_{\text{sca}}$  and  $\beta_{\text{abs}}$  was achieved to find the optimal  $n_1$  and  $k_1$  pair; The RMSD between observation and modelling was calculated as:

$$\text{RMSD} = \sqrt{\left(\frac{\beta_{\text{sca-obs}} - \beta_{\text{sca-mod}}}{\beta_{\text{sca-mod}}}\right)^2 + \left(\frac{\beta_{\text{abs-obs}} - \beta_{\text{abs-mod}}}{\beta_{\text{abs-mod}}}\right)^2} \quad (\text{S1})$$

- Based on the retrieved  $n$  and  $k$  pair, the truncation correction coefficient was calculated as  $C_{\text{sca}}(\lambda) = \beta_{\text{sca}}(\lambda, 0^\circ - 180^\circ) / \beta_{\text{sca,no-tc}}(\lambda, \theta_1 - \theta_2)$ , where  $\beta_{\text{sca,no-tc}}(\lambda, \theta_1 - \theta_2)$  is the measured truncated scattering signal and  $\beta_{\text{sca}}(\lambda, 0^\circ - 180^\circ)$  is calculated with the Mie theory using retrieved  $n$  and  $k$  and SMPS size as an input;
- Sensitivity calculations to the input parameters, as well as the  $C_{\text{ref}}$  variability, were performed to provide the  $n$  and  $k$  uncertainty. Those consisted in repeating the iterative method and retrieving  $n$  and  $k$  by using as input the first and third quartiles, the median and the mean of the scattering and absorption coefficients and number size distribution to take into account the variability of the dataset within the averaged hour time-step and the systematic error of the measurement. The final value for  $n$  and  $k$  were estimated as the average of the  $n$  and  $k$  from the sensitivity tests, and the total uncertainty was set at the standard deviation of the  $n$  and  $k$  from all the tests performed.

## S2. Detailed procedure for CRI retrieval from the GRIMM OPC – SMPS comparison

The following treatment on the GRIMM OPC and SMPS data was applied:

- The GRIMM OPC not CRI corrected data ( $dN(D_{opt})/d\log D_{opt}$ ) were interpolated over the SMPS geometrical diameters path;
- The imaginary part of the refractive index was fixed to that of the optical retrieval at the closest wavelength compared to the operating GRIMM OPC wavelength.
- The optical-to-geometrical correction on the GRIMM OPC size distribution was performed varying the diameters corrections in the [1.33, 1.74] real refractive index range following look up tables in Formenti et al. (2021);
- The root mean squared error (RMSE) and mean absolute error (MAE) between the GRIMM OPC and SMPS  $dN(D_g)/d\log D_g$  were estimated at each iteration after applying the aforementioned corrections;
- The average of the real refractive index on all the values within the 15<sup>th</sup> percentile distribution of RMSE and MAE was calculated;
- The uncertainty on the retrieved  $n$  was calculated performing sensitivity simulations taking into account i) the size distribution statistical error due to counting (detailed in Sec 2.2.3) and ii) the imaginary part uncertainty from the iterative method retrieval.

The RMSE stands for the root mean squared error and was calculated as:

$$RMSE = \sqrt{\frac{\sum \left( \frac{dN}{d\log(D)_{SMPS}} - \frac{dN}{d\log(D)_{GRIMM\ OPC}} \right)^2}{N}} \quad (S2)$$

where  $N$  is the number of points in the overlapping region. The MAE is the mean absolute error and it has been estimated as:

$$MAE = \frac{1}{N} \left| \frac{dN}{d\log(D)_{SMPS}} - \frac{dN}{d\log(D)_{GRIMM\ OPC}} \right| \quad (S3)$$

### S3. Mass concentration threshold for CRI retrieval: optical closure versus OPC–SMPS overlap methods

Figure 2 in the main manuscript shows the 1:1 comparison between the real refractive index retrieved at 780 and 655 nm at PRG and RambForest based on optical closure versus OPC–SMPS overlap method (the time series of the retrieved  $n$  at PRG and RambForest with the two methods is shown in Fig. S10). Considering all data points (panel (a) and (b) of Fig. 2), a slope of 0.77 and 0.23 and a correlation coefficient of 0.82 and 0.15 are obtained respectively for the PRG and RambForest, indicating a limited correlation at forest site. A closer look at the data suggests that periods with very low aerosol load, however, significantly influence the comparison. This is not surprising since the lower the aerosol load, the lower the constraint given by the measured optical signal and number concentration to the retrieval procedure. The correlation significantly improves at the RambForest site (slope of 0.93 and a correlation coefficient of 0.6, panel (d) of Fig. 2), while showing a weak impact on the PRG site (slope of 0.75 and a correlation coefficient of 0.84, panel (c) of Fig. 2), when applying a threshold to the dataset at  $3 \mu\text{g m}^{-3}$ , estimated based on the number concentration from the SMPS and assuming an aerosol uniform density of  $1.4 \text{ g cm}^{-3}$ . This threshold corresponds to a  $\beta_{\text{ext}}$  of  $12 \text{ Mm}^{-1}$  (if a mass extinction efficiency, MEE, of  $4 \text{ m}^2\text{g}^{-1}$  is assumed), corresponding to the 25<sup>th</sup>, 35<sup>th</sup> and 52<sup>th</sup> percentiles of the  $\beta_{\text{ext}}$  distribution at PRG, SIRTa and RambForest sites, respectively. This analysis, which compares the real refractive index data derived based on independent calculations and different inputs (SMPS,  $\beta_{\text{abs}}$  and  $\beta_{\text{sca}}$  on one side, and SMPS versus OPC on the other), suggests that a minimum in the aerosol load is necessary to provide a well constrained retrieval. Applying a  $3 \mu\text{g m}^{-3}$  threshold reduces the total number of valid CRI retrieval by 5%, 37% and 43%, respectively, for the urban, peri–urban and forest sites, while the robustness of the retrieved dataset is increased.

INPUTS	SIMULATION LABELS	SITE	RESULT
dN(D <sub>g</sub> )/dlogD <sub>g</sub> from SMPS  β <sub>sca</sub>  β <sub>abs</sub>	mean, q1, median, q3, errp, errm	Paris Rive Gauche (PRG)  SIRTA  Rambouillet	n-ik (mean±SD)

**Table S1: List of all simulations performed using the different inputs to retrieve the final CRI. The simulation labels represent the attributed name to the sensitivity tests performed: “mean” represents the test using the hourly mean inputs, “q1” represents the test using 1st quartile values of the inputs, “q3” represents the test using 3rd quartile values of the inputs, “median” represents the test using the median values of the inputs, “errp” represents the test performed on the median values plus the instrumental error due to noise and SD of the inputs, “errm” represents the test performed on the median values minus the instrumental error due to noise and SD of the inputs. The final CRI is retrieved as the mean σ±SD.**

Wind direction	SSA $\pm$ SD			n $\pm$ SD			k $\pm$ SD		
	PRG	SIRTA	Ramb Forest	PRG	SIRTA	Ramb Forest	PRG	SIRTA	Ramb Forest
N	0.73 $\pm 0.08$	0.79 $\pm 0.06$	0.86 $\pm 0.03$	1.40 $\pm 0.07$	1.56 $\pm 0.05$	1.48 $\pm 0.05$	0.035 $\pm$ 0.016	0.039 $\pm$ 0.010	0.021 $\pm 0.004$
NNE	0.77 $\pm 0.06$	0.80 $\pm 0.07$	0.85 $\pm 0.03$	1.39 $\pm 0.05$	1.52 $\pm 0.08$	1.50 $\pm 0.03$	0.027 $\pm$ 0.007	0.038 $\pm 0.015$	0.023 $\pm 0.004$
NE	0.75 $\pm 0.09$	0.78 $\pm 0.08$	0.83 $\pm 0.03$	1.40 $\pm 0.05$	1.50 $\pm 0.07$	1.48 $\pm 0.06$	0.031 $\pm 0.015$	0.040 $\pm 0.014$	0.024 $\pm$ 0.005
ENE	0.78 $\pm 0.07$	0.79 $\pm 0.07$	0.82 $\pm 0.04$	1.40 $\pm 0.05$	1.51 $\pm 0.07$	1.50 $\pm 0.05$	0.025 $\pm 0.008$	0.039 $\pm 0.012$	0.028 $\pm 0.007$
E	0.77 $\pm 0.10$	0.73 $\pm 0.11$	0.80 $\pm 0.05$	1.38 $\pm 0.06$	1.50 $\pm 0.06$	1.50 $\pm 0.04$	0.031 $\pm 0.015$	0.051 $\pm 0.031$	0.032 $\pm 0.008$
ESE	0.73 $\pm 0.08$	0.76 $\pm 0.08$	0.82 $\pm 0.04$	1.42 $\pm 0.04$	1.51 $\pm 0.09$	1.53 $\pm 0.03$	0.038 $\pm 0.015$	0.044 $\pm 0.019$	0.030 $\pm$ 0.008
SE	0.71 $\pm 0.10$	0.75 $\pm 0.12$	0.85 $\pm 0.05$	1.43 $\pm 0.04$	1.55 $\pm 0.06$	1.54 $\pm 0.04$	0.044 $\pm 0.024$	0.059 $\pm 0.029$	0.027 $\pm$ 0.004
SSE	0.69 $\pm 0.11$	0.81 $\pm 0.10$	0.88 $\pm 0.05$	1.42 $\pm 0.04$	1.53 $\pm 0.06$	1.55 $\pm 0.02$	0.049 $\pm 0.030$	0.065 $\pm 0.026$	0.021 $\pm$ 0.003
S	0.70 $\pm 0.08$	0.84 $\pm 0.05$	0.90 $\pm 0.02$	1.42 $\pm 0.06$	1.56 $\pm 0.04$	1.51 $\pm 0.08$	0.043 $\pm 0.013$	0.031 $\pm 0.014$	0.018 $\pm 0.005$
SSW	0.69 $\pm 0.10$	0.84 $\pm 0.05$	0.90 $\pm 0.03$	1.41 $\pm 0.06$	1.55 $\pm 0.05$	1.51 $\pm 0.02$	0.050 $\pm 0.021$	0.022 $\pm 0.008$	0.021 $\pm 0.002$
SW	0.66 $\pm 0.10$	0.85 $\pm 0.05$	0.89 $\pm 0.03$	1.39 $\pm 0.06$	1.55 $\pm 0.06$	1.51 $\pm 0.05$	0.051 $\pm 0.026$	0.024 $\pm 0.008$	0.020 $\pm 0.004$
WSW	0.67 $\pm 0.10$	0.83 $\pm 0.06$	0.90 $\pm 0.03$	1.39 $\pm 0.04$	1.51 $\pm 0.06$	1.49 $\pm 0.06$	0.044 $\pm 0.022$	0.024 $\pm 0.006$	0.018 $\pm 0.005$
W	0.73 $\pm 0.12$	0.83 $\pm 0.06$	0.87 $\pm 0.04$	1.44 $\pm 0.06$	1.50 $\pm 0.07$	1.54 $\pm 0.10$	0.040 $\pm 0.024$	0.024 $\pm 0.006$	0.021 $\pm 0.006$
WNW	0.72 $\pm 0.12$	0.81 $\pm 0.08$	0.87 $\pm 0.04$	1.42 $\pm 0.07$	1.56 $\pm 0.05$	1.48 $\pm 0.11$	0.038 $\pm 0.018$	0.027 $\pm 0.006$	0.020 $\pm 0.004$
NW	0.82 $\pm 0.10$	0.85 $\pm 0.08$	0.89 $\pm 0.03$	1.43 $\pm 0.06$	1.51 $\pm 0.07$	1.52 $\pm 0.02$	0.033 $\pm 0.021$	0.032 $\pm 0.010$	0.018 $\pm 0.006$
NNW	0.77 $\pm 0.10$	0.82 $\pm 0.06$	0.86 $\pm 0.04$	1.41 $\pm 0.08$	1.56 $\pm 0.04$	1.50 $\pm 0.04$	0.033 $\pm 0.012$	0.033 $\pm 0.009$	0.023 $\pm 0.007$

**Table S2: Single scattering albedo (SSA) and complex refractive index averages  $\pm$ SD at 520 nm for the urban (PRG), peri-urban (SIRTA) and forest (RambForest) sites and under different wind direction regimes.**

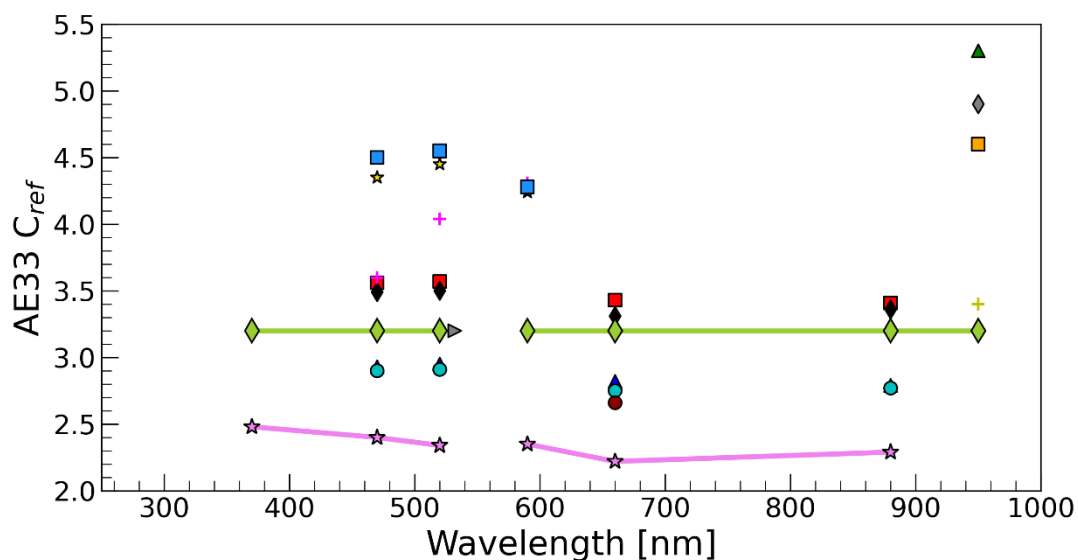
160

165

170

Study	$\lambda$ (nm)	Characteristics	Type	Localization	Real	Imaginary
Espinosa et al., 2019	532	Biogenic	Airborne	USA	1.51±0.027	0.0040±0.0009
		Urban			1.52±0.026	0.0050±0.0012
		Biomass Burning			1.55±0.024	0.0070±0.0016
Aldhaif et al., 2018	532	Dry Aerosol	Airborne	Mexico, USA	1.42-1.60	
Shingler et al., 2016	532	Dry Aerosol	Airborne	Mexico, USA	1.52-1.54	
Zhang et al., 2016	532	Urban	In-situ	Guangzhou, China	1.47-1.53	
Zhang et al., 2013	550	Urban	In-situ	Hefei, China	1.50	0.025
J.-C. Raut and P. Chazette, 2008	532	PBL Mean	Airborne	Paris, France	1.51±0.02	0.017±0.003
		Internal Mixing (19-20 July 2000)			1.53	0.02
		External Mixing (19-20 July 2000)			1.54	0.018
		Aerosol over Paris area			1.46-1.48	
		Downwind of Paris (outside Paris plume)			1.50	0.013
		Upwind of Paris			1.48	0.020
		Aged from Great-Britain			1.48-1.50	
		Rural over Paris			1.50	
J.-C. Raut and P. Chazette, 2007	532	Urban	In-situ	Paris, France	1.59	0.04
Ebert et al., 2004	550	Urban influenced air masses	In-situ	Feldberg, Germany	1.60-1.73	0.034-0.086
		Rural influenced air masses			1.54-1.61	0.001-0.021
Ebert et al., 2002	550	Urban	In-situ	Berlin, Germany	1.52-1.57	0.031-0.057
Muller et al., 2002	532	Pollution plumes over the Atlantic Ocean	In-situ	Portugal	1.49-1.63	0.001-0.019
Ferrare et al, 1998	532	Wet aerosol	In-situ	Oklahoma, USA	1.4-1.5	
Ferrare et al, 1998	532	Dry aerosol			1.37-1.4	

Table S3: Literature survey at 532 nm and 550 nm for the real and imaginary part of the complex refractive index.



- |                             |                               |                        |
|-----------------------------|-------------------------------|------------------------|
| ■ Bernardoni et al, 2021 a) | + Kalbermatter et al, 2022 a) | ★ Laing et al, 2020 a) |
| ◆ Bernardoni et al, 2021 b) | □ Kalbermatter et al, 2022 b) | + Laing et al, 2020 b) |
| ▲ Bernardoni et al, 2021 c) | ◆ Kalbermatter et al, 2022 c) | ■ Laing et al, 2020 c) |
| ● Bernardoni et al, 2021 d) | ▲ Kalbermatter et al, 2022 d) | ◆ Muller et al, 2015   |
| ★ Moschos et al, 2021       | ● Valentini et al, 2020       | ► Drinovec et al, 2022 |

Figure S1: Multiple scattering coefficient  $C_{ref}$  values from the recent literature as a function of the wavelength for the dual spot AE33 aethalometer. The (Bernardoni et al., 2021) different cases represent a) daytime polar photometer (PP), b) nighttime PP, c) daytime PaM (PP as Multi Angle Absorption Photometer), d) nighttime PaM approaches. The (Kalbermatter et al., 2022) different cases report  $C_{ref}$  values at different SSA: a) 0.03, b) 0.13, c) 0.5, and d) 0.68. (Laing et al., 2020) different cases obtained in Oregon considering a) all the aerosol species, b) only biomass burning events, and c) only non-biomass burning events.

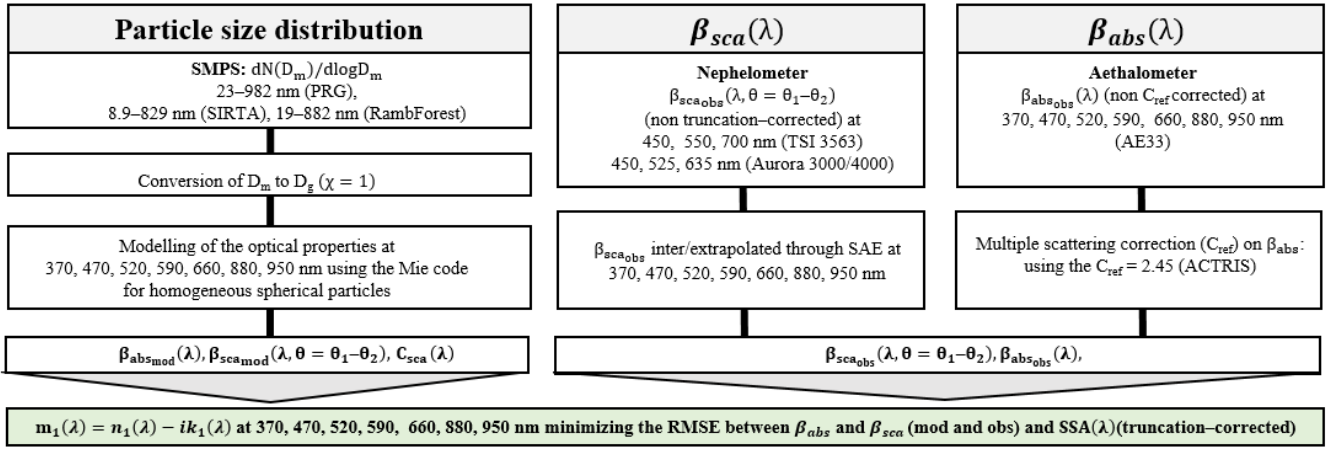
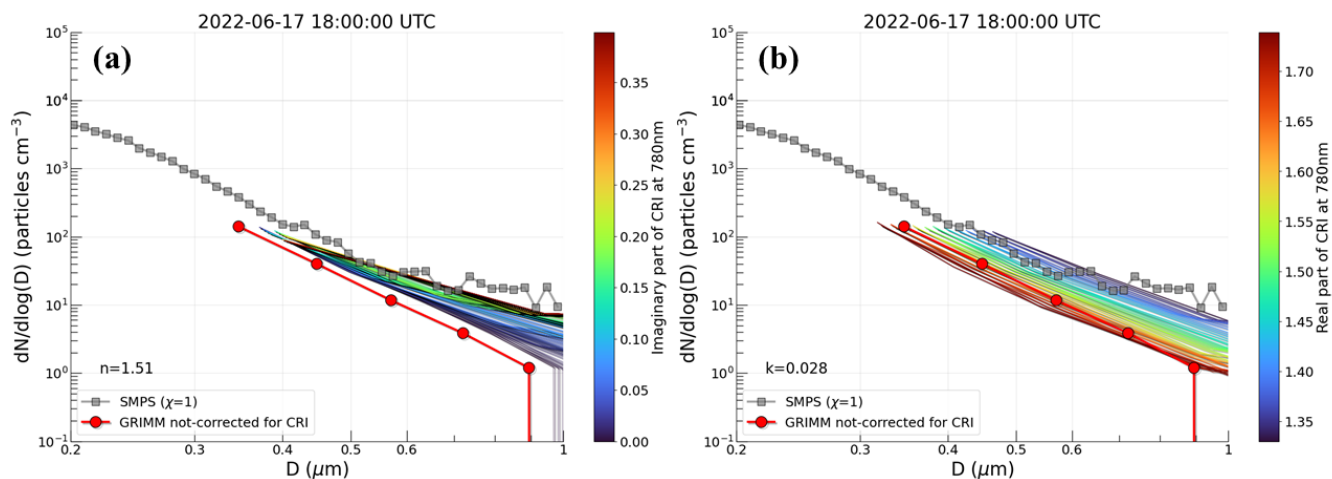


Figure S2: Flowchart of optical complex refractive index retrieval (CRI,  $m=n-ik$ ) by means of the iterative method. See main text and Text S1 for details. The  $dN(D_m)/d\log D_m$  is the SMPS particle size distribution measured through the mobility diameter ( $D_m$ ) range. The  $\beta_{sca}(\lambda, \theta_1 - \theta_2)$  is the spectral aerosol scattering coefficient integrated within the nephelometer measured angles  $\theta_1$  and  $\theta_2$ , which corresponds to  $\beta_{sca, no-trunc}(\lambda, \theta_1 - \theta_2)$  in the main text. The subscript obs and mod represent respectively the modelled and the observed parameter. The  $\beta_{sca}(\lambda, 0^\circ - 180^\circ)$  is the spectral aerosol scattering coefficient integrated over the  $0^\circ - 180^\circ$  range. The  $\beta_{abs}(\lambda)$  is the measured spectral aerosol absorption coefficient, and  $C_{ref}$  is the multiple scattering parameter. The  $C_{sca}(\lambda)$  is the spectral truncation correction coefficient for the measured  $\beta_{sca}(\lambda, \theta_1 - \theta_2)$ .  $m_1(\lambda)$  and  $SSA(\lambda)$  are the retrieved spectral complex refractive index and single scattering albedo.





**Figure S3: Sensitivity of the GRIMM OPC (model 1.108) particle size distribution ( $<1\mu\text{m}$ )  $dN(D_{\text{opt}})/d\log D_{\text{opt}}$  at the Paris Rive Gauche (PRG) site to a) the imaginary part of the CRI used for the optical-to-geometrical diameters correction, fixing the real part at the optical retrieved value of 1.51, and b) the real part of the CRI used for the optical-to-geometrical diameters correction, fixing the imaginary part at the optical retrieved value of 0.028, for observations taken on the 17 June 2022 at 18 UTC. Grey squares represent the SMPS particle size distribution. The red circles, the GRIMM OPC not-corrected size distribution, while the coloured lines are CRI corrected OPC sizes. The colour code refers to the variability of the imaginary and real part respectively for a) and b).**

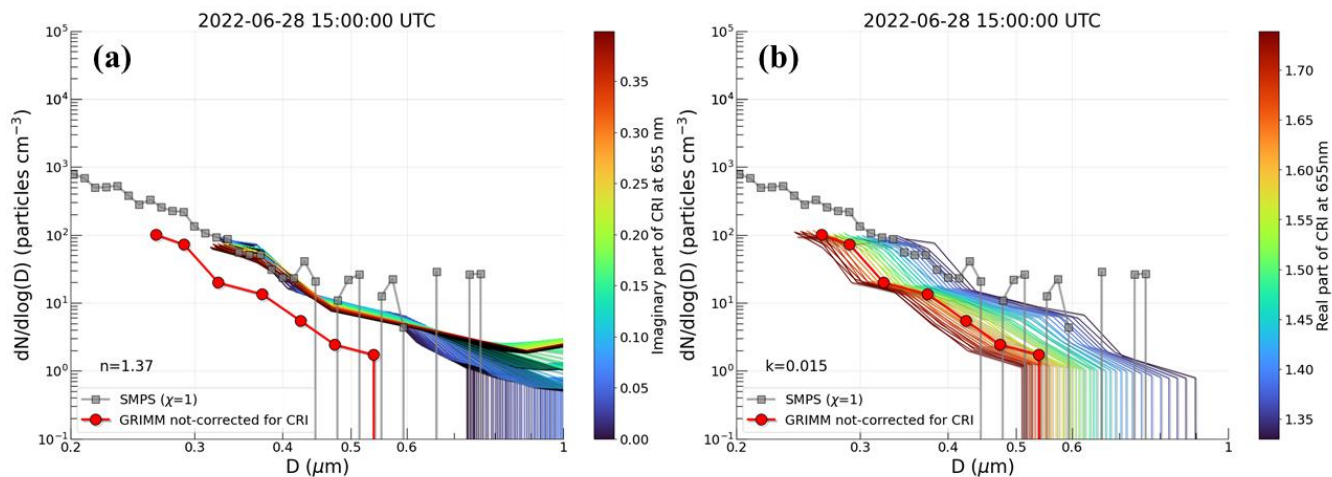
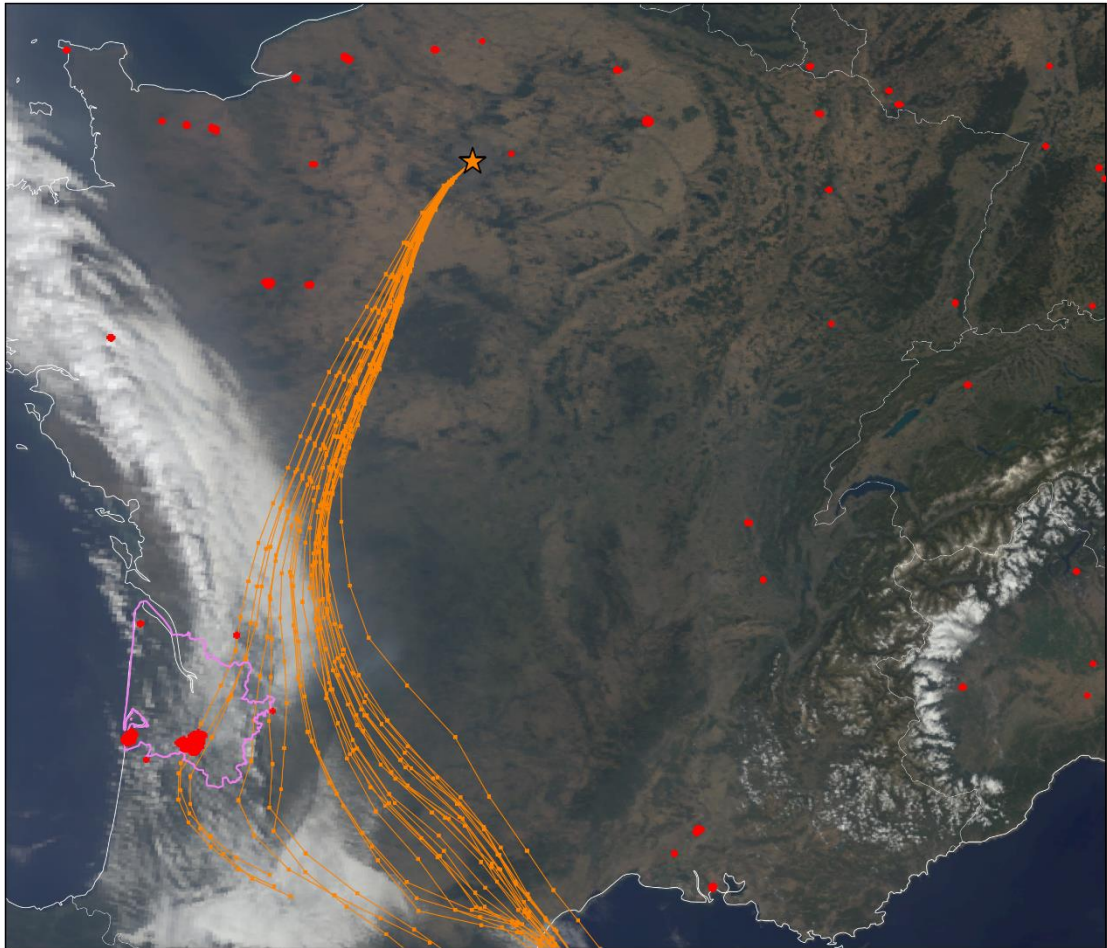
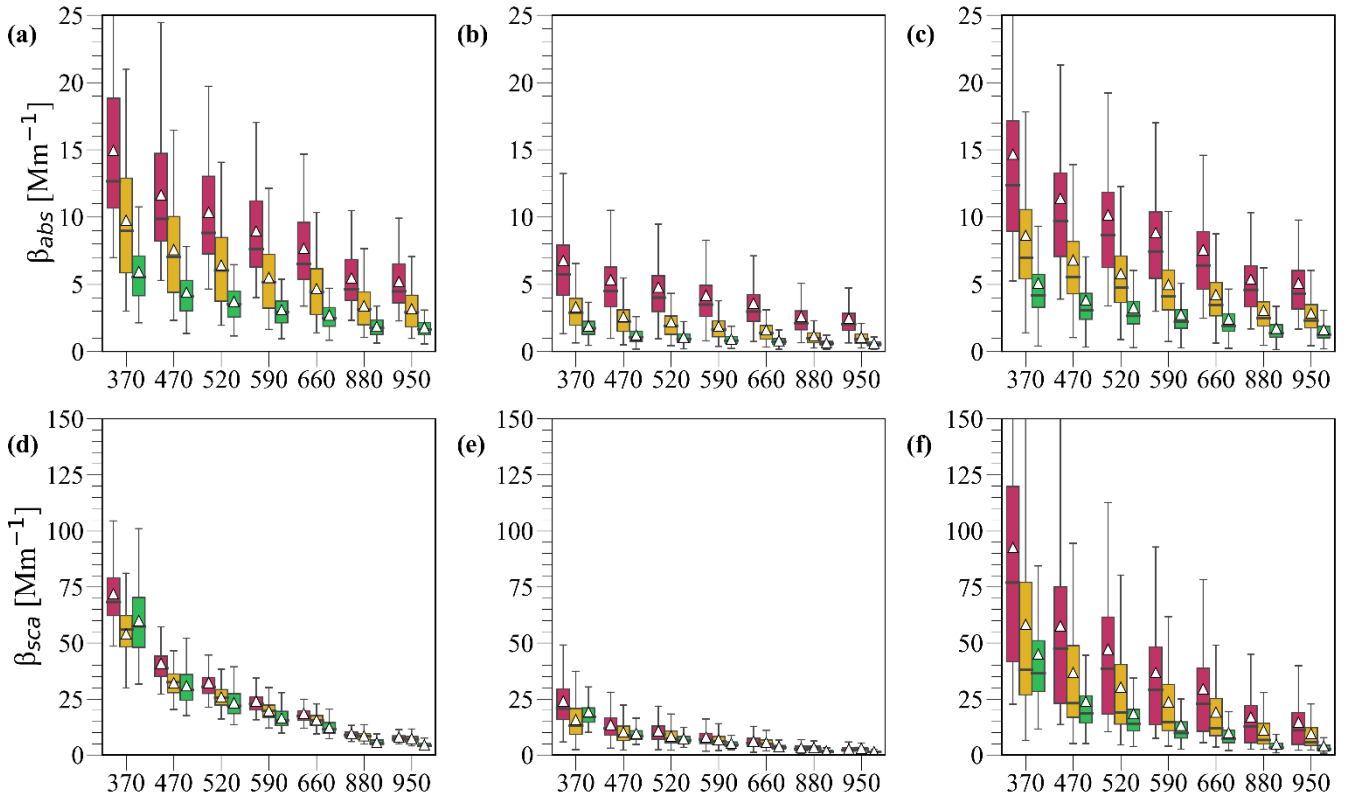


Figure S4: Sensitivity of the GRIMM OPC (model 1.109) particle size distribution ( $<1\mu\text{m}$ )  $dN(D_{\text{opt}})/d\log D_{\text{opt}}$  at the Rambouillet (RambForest) site to a) the imaginary part of the CRI used for the optical-to-geometrical diameters correction, fixing the real part at the optical retrieved value of 1.51, and b) the real part of the CRI used for the optical-to-geometrical diameters correction, fixing the imaginary part at the optical retrieved value of 0.028, for observations taken on the 17 June 2022 at 18 UTC. Grey squares represent the SMPS particle size distribution. The red circles, the GRIMM OPC not-corrected size distribution, while the coloured lines are CRI corrected OPC sizes. The colour code refers to the variability of the imaginary and real part respectively for a) and b).



290

**Figure S5: Illustration of the long-range fire transport occurred on July 19, 2022, from southern France to the Ile-de-France region. The background image represents a true color image acquired by the Moderate Resolution Imaging Spectroradiometer (MODIS) Terra satellite on the July 19 2022 at 10:00 UTC. The Level 1B Calibrated Radiances at 1 km resolution (the MOD021KM product) have been used. Red dots represent the active fires from the MODIS Terra Thermal Anomalies/Fire 8-Day L3 product (MOD14A2) between the July 12 and July 19 2022. Orange lines represents the ensemble 24h backtrajectories from the WRF-HYSPLIT model simulation performed during the ACROSS field campaign 2022 (Siour and Di Antonio, 2023).**



295 **Figure S6: Wavelength dependence of  $\beta_{abs}$ , and  $\beta_{sca}$  and splitted by the different sites and under the first heatwave, the clean period and the second heatwave: a) and d), for the Paris Rive gauche (PRG) site; b) and e) for the SIRTA site; c), and f) for the Rambouillet (RambForest) site. The absorption and scattering coefficients are decreasing with the wavelength for all the three sites, showing an urban-to-rural gradient. The white triangles represent the mean values, while the median is been reported as the line crossing the boxplot. Outliers are not shown for the sake of readability.**

300

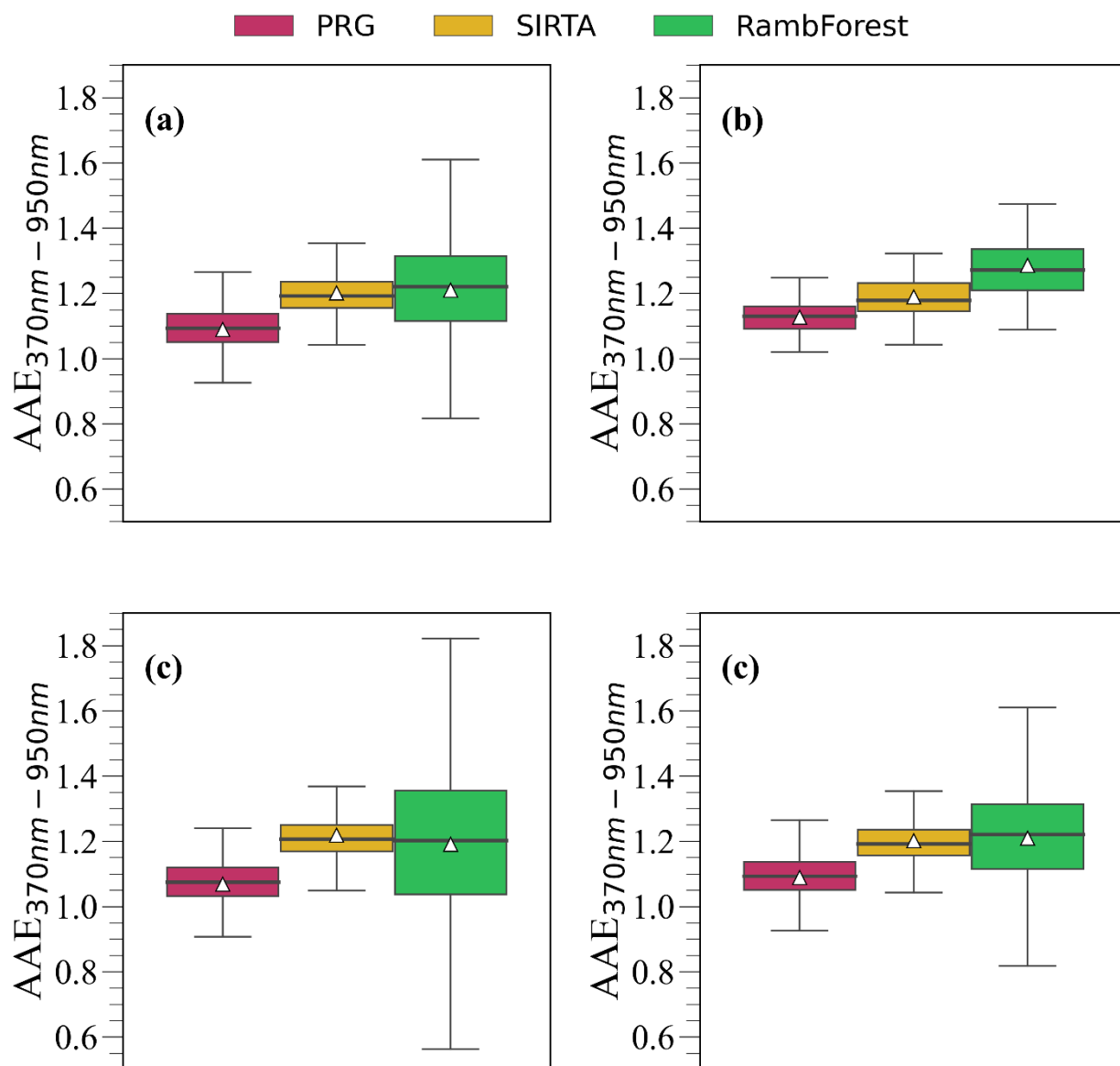
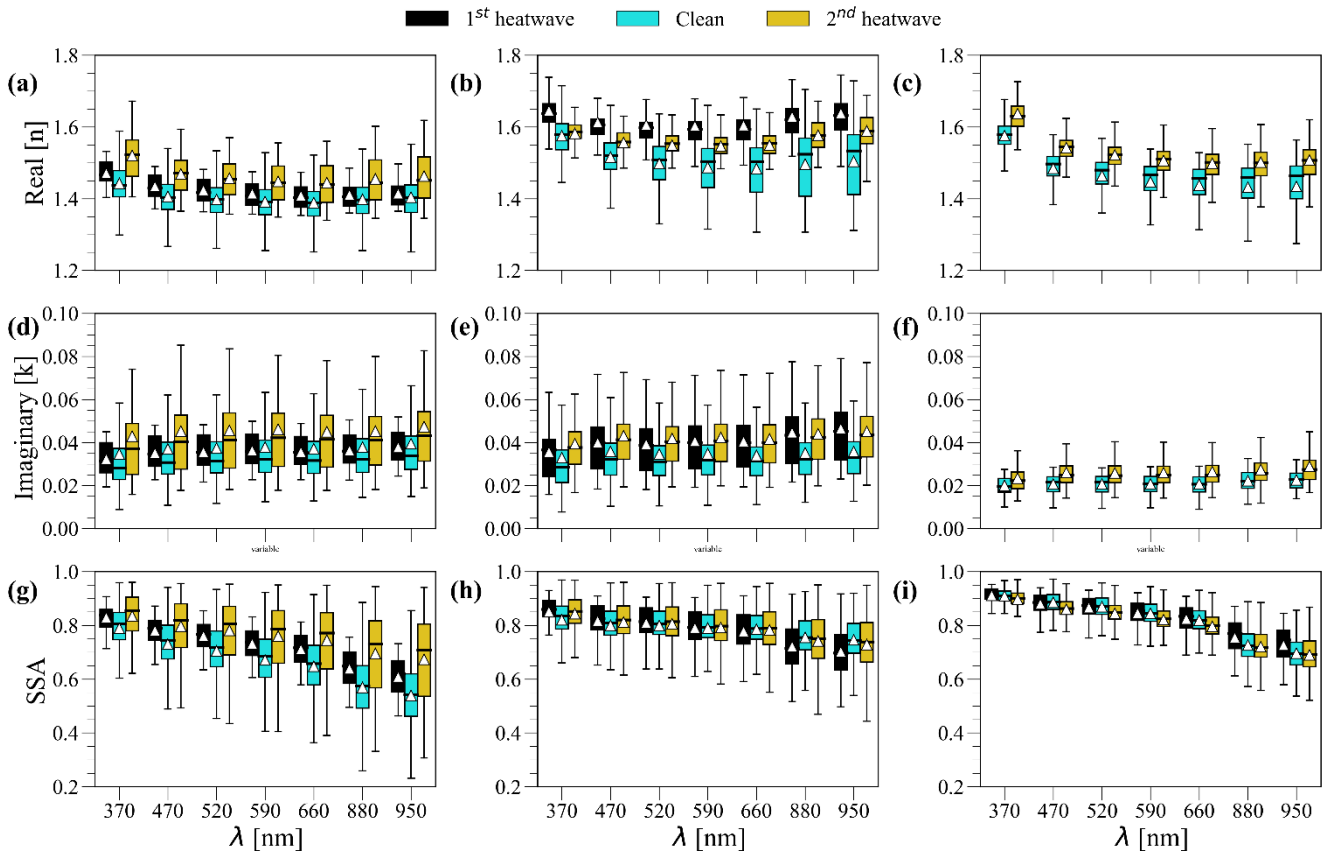


Figure S7: Absorption angstrom exponent between 370 and 950 nm variability for (a) full period (b) first heatwave (c) clean period and (d) second heatwave for the PRG, Sirta and RambForest sites. Higher values are observed at the forest site compared to the urban site. Black lines represent the boxplot median, while white triangles represent the boxplot mean.

305

310



**Figure S8: Wavelength dependence of the single scattering albedo (SSA) and complex refractive index (CRI) for all the available points in the period under investigation for the PRG (panels (a), (d), (g)), SIRTA (panels (b), (e), (h)), RambForest (panels (c), (f), (i)) ground-based sites. White triangles show the average value, while black lines show the median values. Outliers are not shown for the sake of readability.**

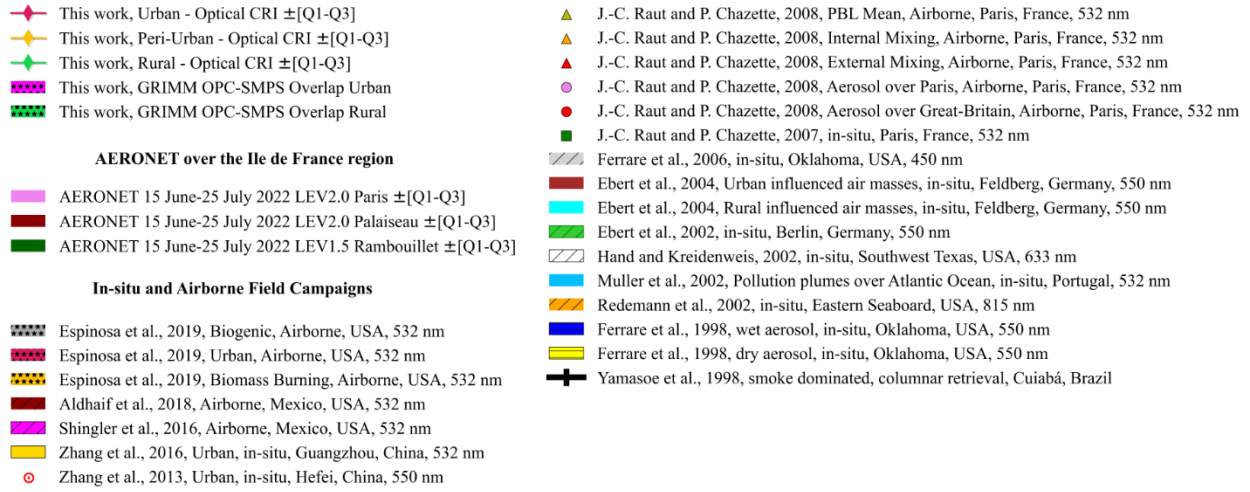
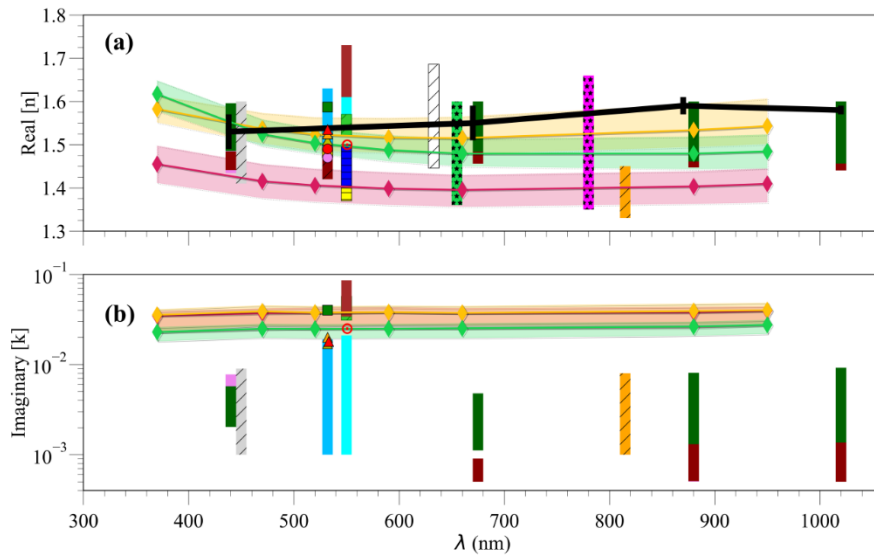
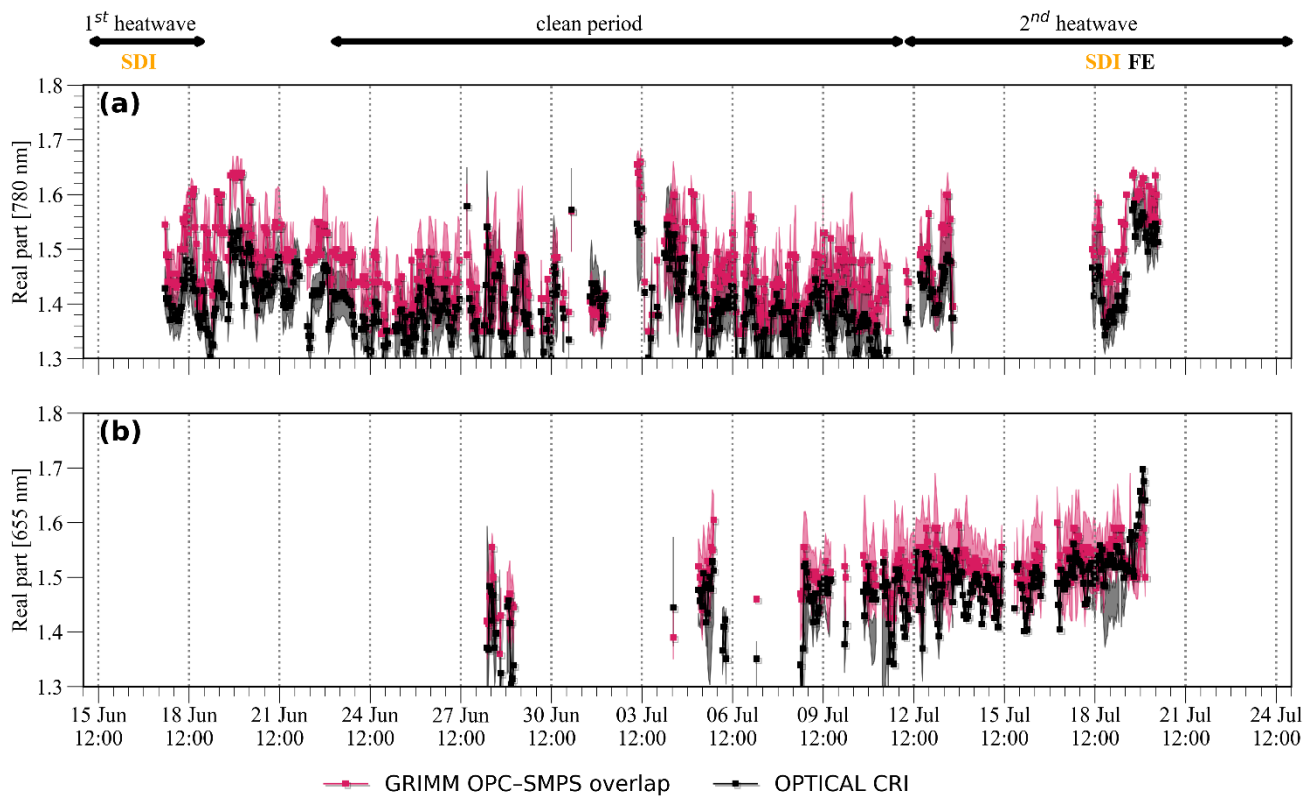


**Figure S9: Comparison of the results obtained in this work with literature surveys of the (a) real ( $n$ ) and (b) imaginary ( $k$ ) part of the complex refractive index (CRI). Mean (solid line), 25th percentile (dotted line), 75th percentile (dashed line) and interquartile range (coloured area) of the CRI at Paris Rive Gauche (PRG, urban), Sirta (peri-urban) and Rambouillet (RambForest) sites for the entire ACROSS period 2022 are shown. The legend identifies the line styles used for the literature works. Note that for the  $k$  values the line for PRG is mainly hidden under that of Sirta.**



360 **Figure S10:** Time series of the real part of the refractive index retrieved at a) the PRG (urban) site and b) the RambForest (forest) site using the two methods detailed in Sec. 3 and Text S1 and S2. Shaded area represents the uncertainty of the retrievals.

365



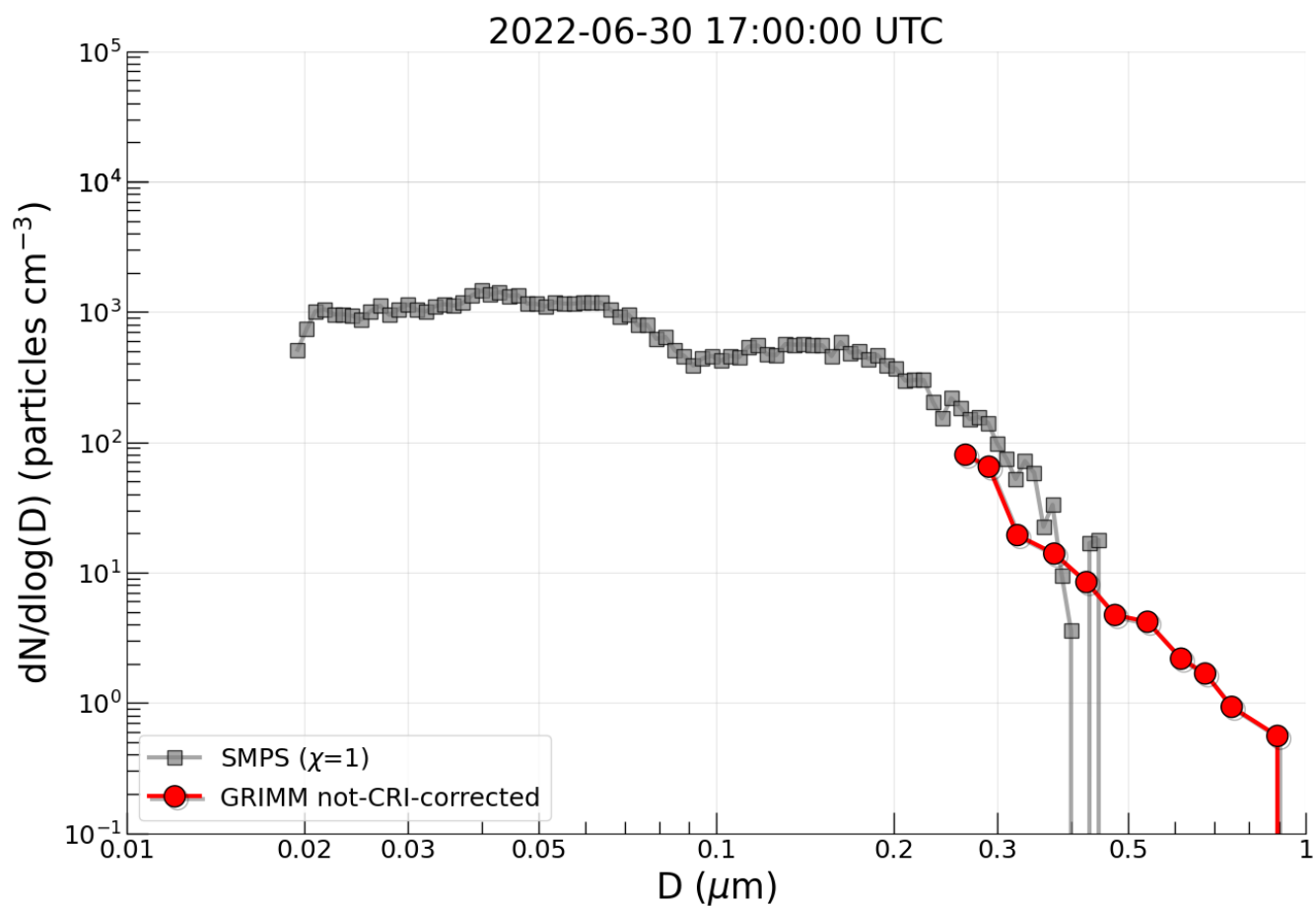


**Figure S11: SMPS and GRIMM OPC not-CRI-corrected particle size distribution ( $<1 \mu\text{m}$ )  $dN(D)/d\log D$  hourly median measured at RambForest site for the 30 June at 17 UTC. SMPS shows no particles above  $0.5 \mu\text{m}$ , compared to the OPC.**

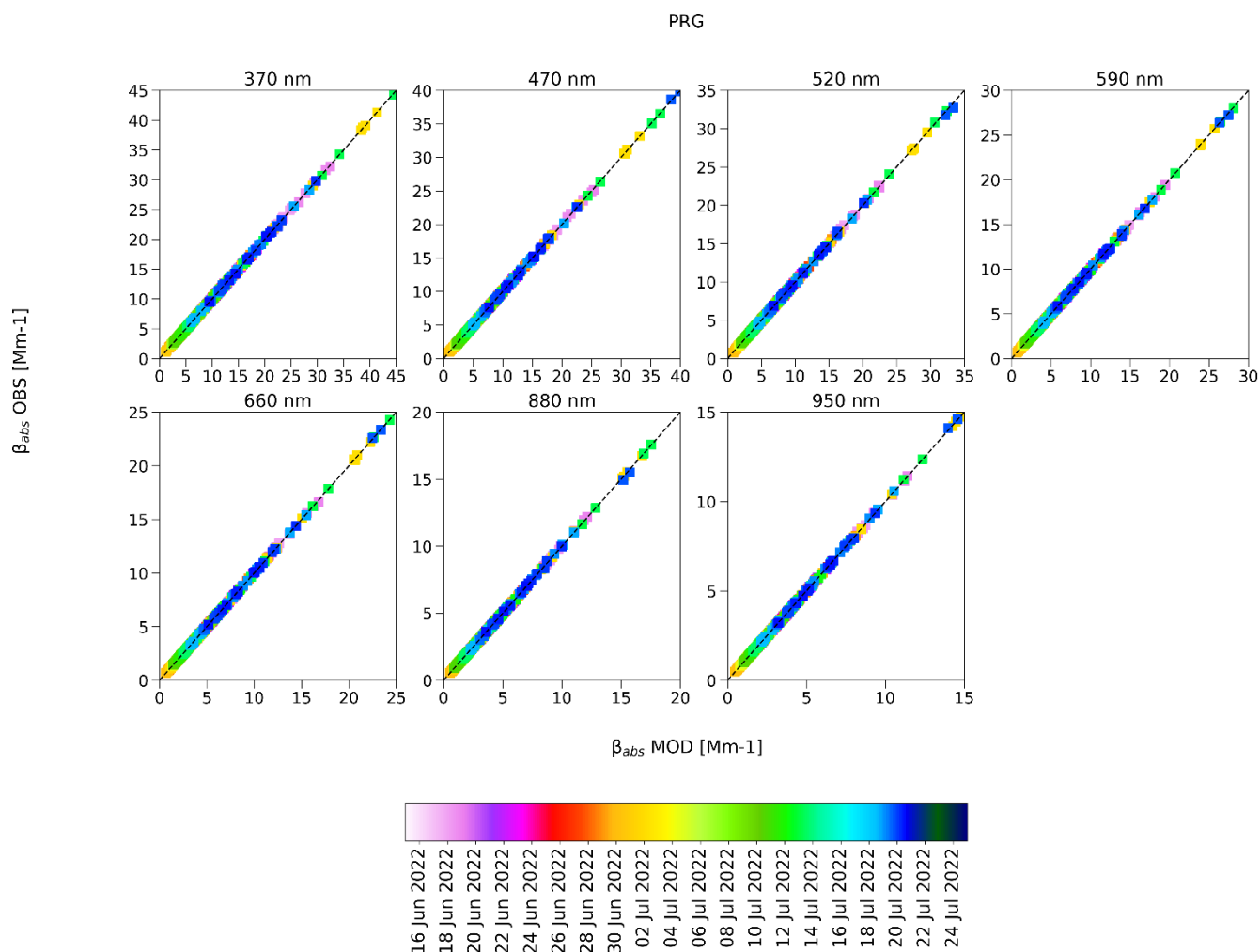


**Figure S12:** Scatter plot of the hourly median observed absorption coefficient vs modelled at seven different wavelengths and during the entire ACROSS campaign at the Paris Rive Gauche (urban site). The colorbar represents the time. The absorption coefficient has been calculated using a Mie code for spherical particles varying the real part ( $n$ ) and imaginary part ( $k$ ) in the  $[1.3, 2]$  and  $[0, 0.2]$  respectively. The modelled value represents the value that minimizes the root mean squared difference (RMSD) of Eq. 4. Only SMPS data has been taken into account.

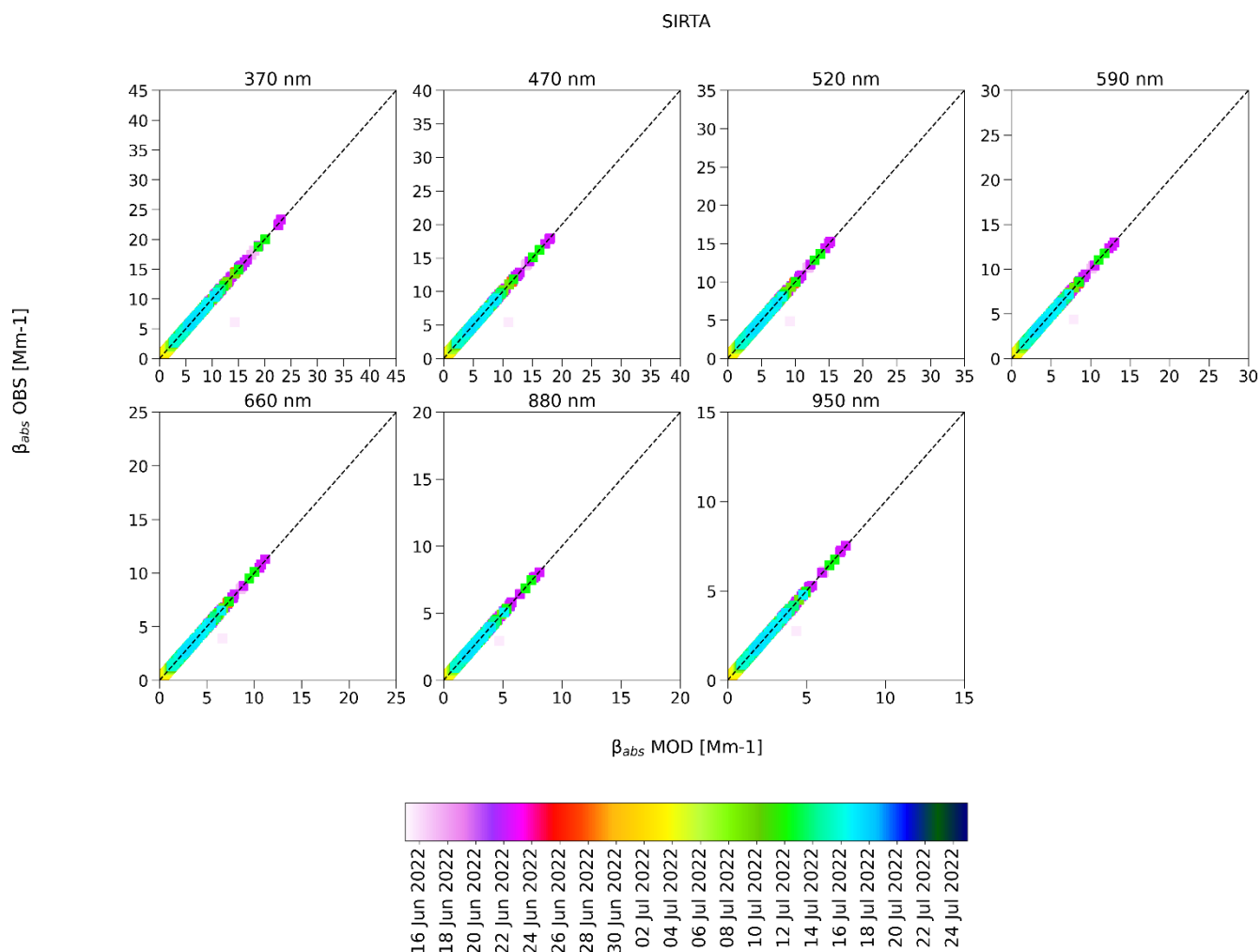
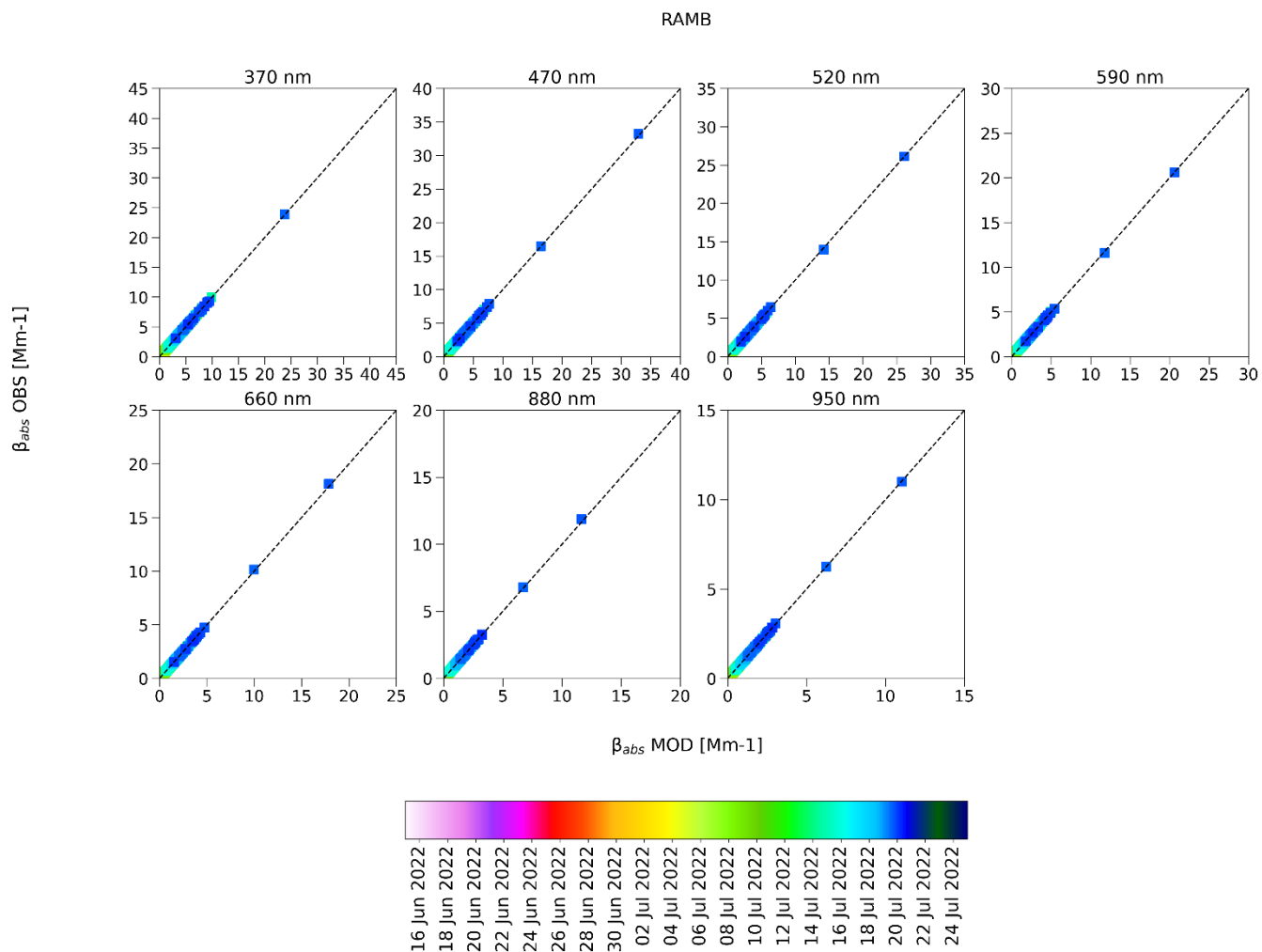
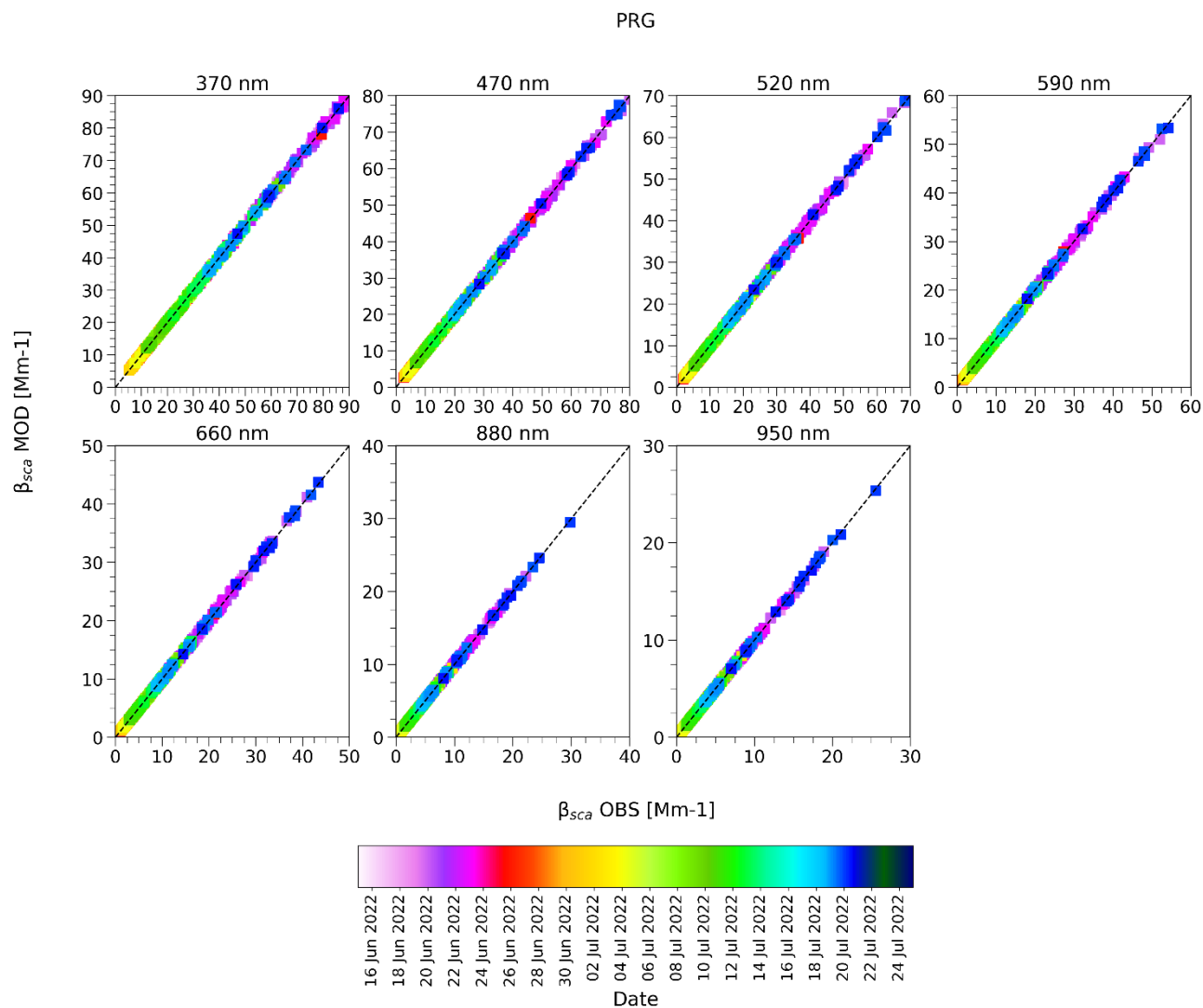


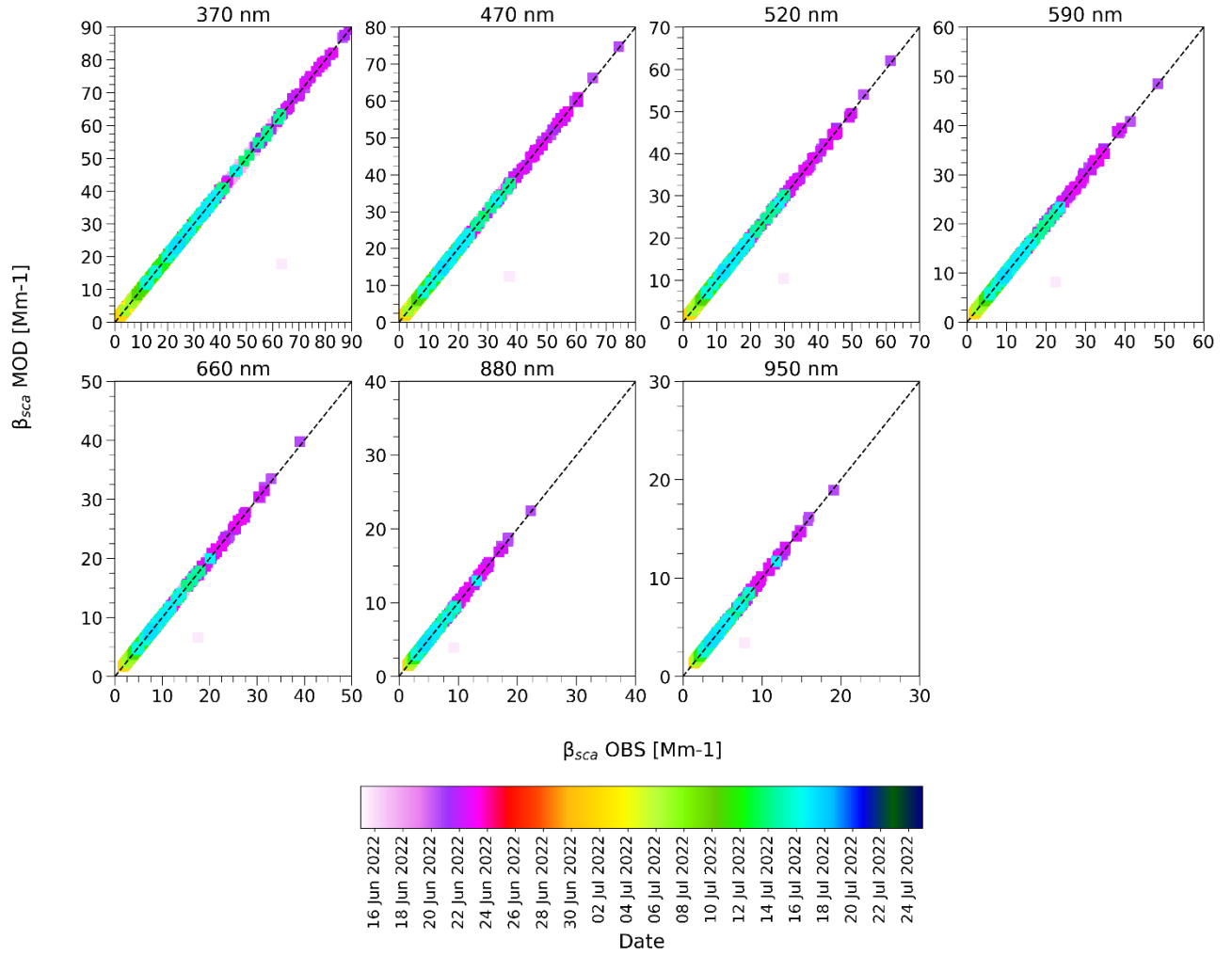
Figure S13: Scatter plot of the hourly median observed absorption coefficient vs modelled at seven different wavelengths and during the entire ACROSS campaign at the SIRTA (peri-urban site). The colorbar represents the time. The absorption coefficient has been calculated using a Mie code for spherical particles varying the real part ( $n$ ) and imaginary part ( $k$ ) in the  $[1.3, 2]$  and  $[0, 0.2]$  respectively. The modelled value represents the value that minimizes the root mean squared difference (RMSD) of Eq. 4. Only SMPS data have been taken into account.



**Figure S14:** Scatter plot of the hourly median absorption coefficient observed vs modelled at seven different wavelengths and during the entire ACROSS campaign at the Rambouillet (forest site). The colorbar represents the time. The absorption coefficient has been calculated using a Mie code for spherical particles varying the real part ( $n$ ) and imaginary part ( $k$ ) in the  $[1.3, 2]$  and  $[0, 0.2]$  respectively. The modelled value represents the value that minimises the root mean squared difference (RMSD) of Eq. 4. Only SMPS data have been taken into account.



**Figure S15: Scatter plot of the hourly median observed scattering coefficient vs modelled at seven different wavelengths and during the entire ACROSS campaign at the Paris Rive Gauche (urban site). The colorbar represents the time. The scattering coefficient has been calculated using a Mie code for spherical particles varying the real part ( $n$ ) and imaginary part ( $k$ ) in the  $[1.3,2]$  and  $[0,0.2]$  respectively. The modelled value represents the value that minimises the root mean squared difference (RMSD) of Eq. 4. Only SMPS data has been taken into account.**



410 **Figure S16: Scatter plot of the hourly median observed scattering coefficient vs modelled at seven different wavelengths and during the entire ACROSS campaign at the SIRTA (peri-urban site). The colorbar represents the time. The scattering coefficient has been calculated using a Mie code for spherical particles varying the real part ( $n$ ) and imaginary part ( $k$ ) in the [1.3,2] and [0,0.2] respectively. The modelled value represents the value that minimises the root mean squared error of Eq. x. Only SMPS data has been taken into account.**

415

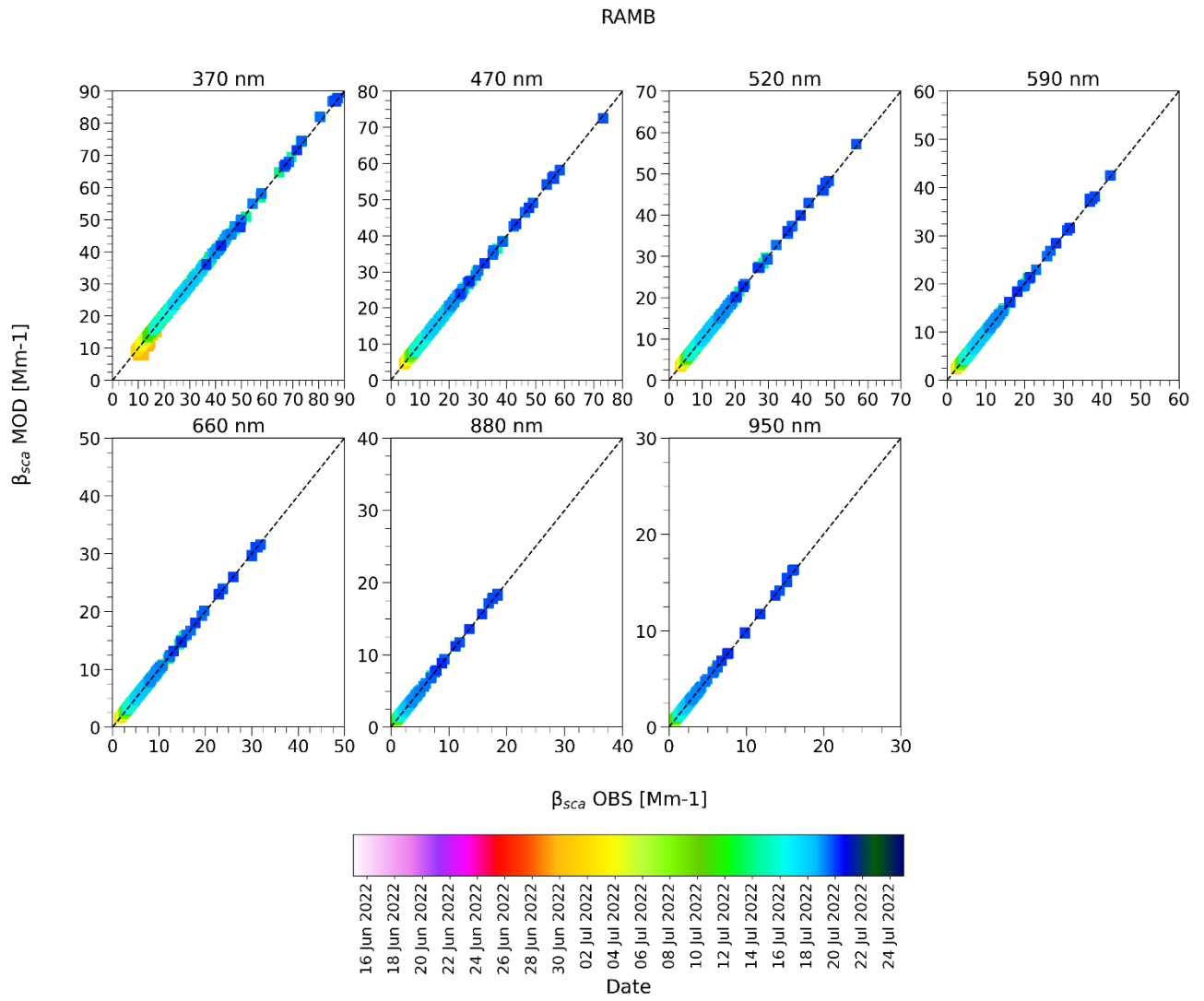
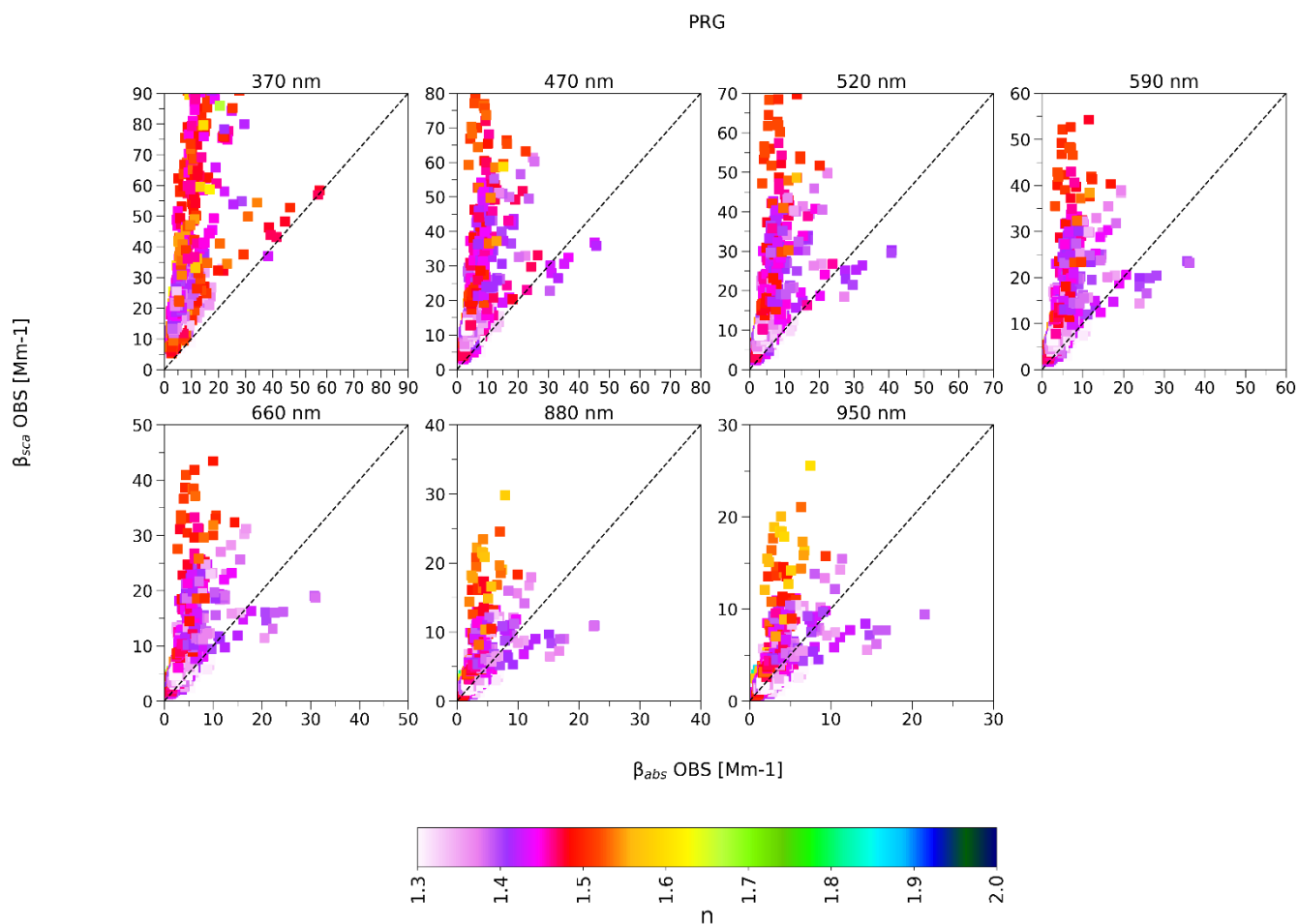


**Figure S17:** Scatter plot of the hourly median observed scattering coefficient vs modelled at seven different wavelengths and during the entire ACROSS campaign at the Rambouillet (forest site). The colorbar represents the time. The scattering coefficient has been calculated using a Mie code for spherical particles varying the real part ( $n$ ) and imaginary part ( $k$ ) in the  $[1.3, 2]$  and  $[0, 0.2]$  respectively. The modelled value represents the value that minimises the root mean squared difference (RMSD) of Eq. 4. Only SMPS data has been taken into account.

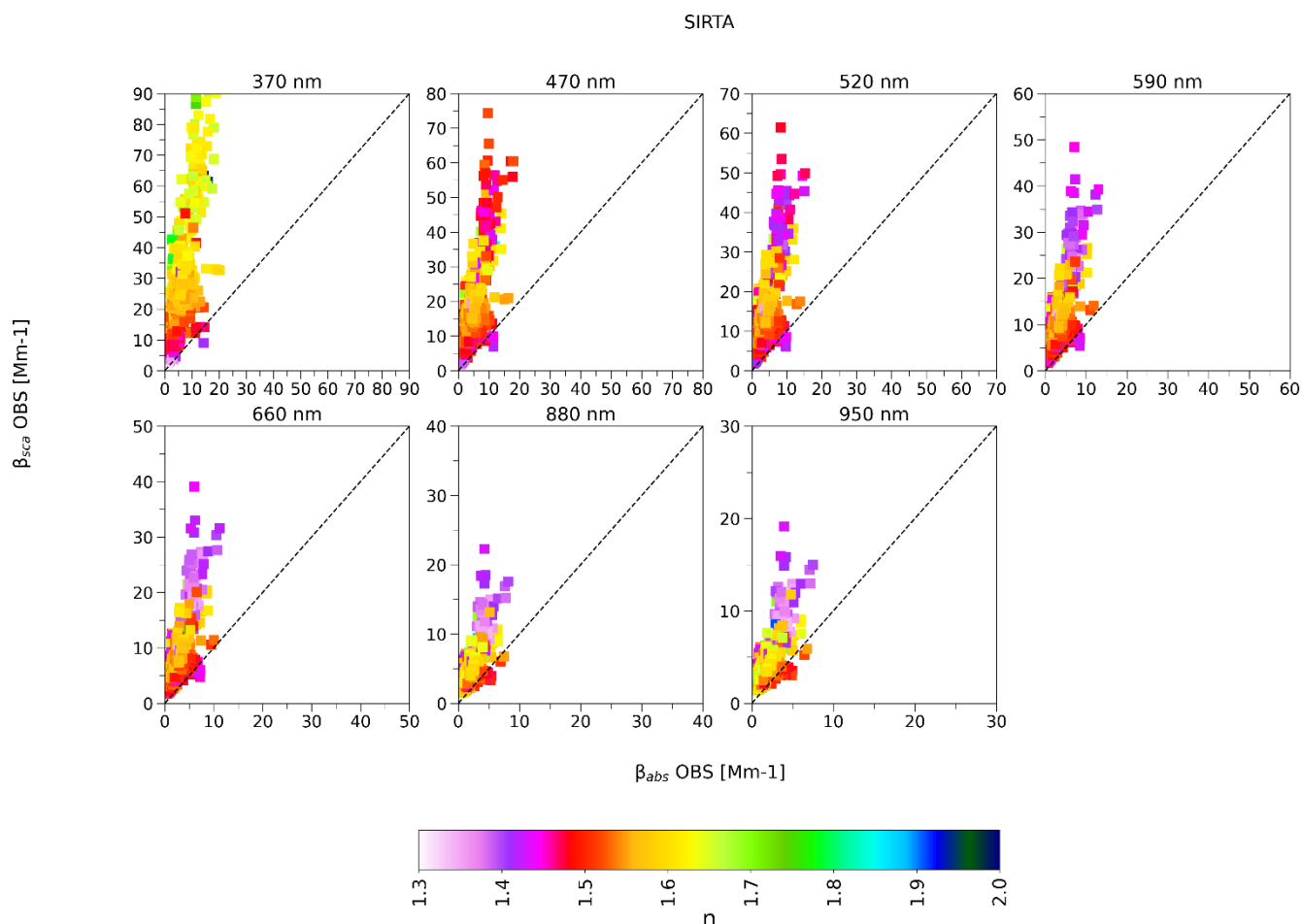


425

**Figure S18:** Scatter plot of hourly median observed scattering and absorption coefficient at seven different wavelengths and during the entire ACROSS campaign at the Paris Rive Gauche (urban site). The colours represent the simulated real ( $n$ ) part of CRI simulated using a Mie code for spherical particles varying  $n$  and  $k$  in the [1.3,2] and [0,0.2] respectively. The modelled value represents the value that minimizes root mean squared difference (RMSD) of Eq. 4. Only SMPS data has been taken into account for optical calculations.

430





435 **Figure S19:** Scatter plot of hourly median observed scattering and absorption coefficient at seven different wavelengths and during the entire ACROSS campaign at the SIRTA (peri-urban site). The colours represent the simulated  $n$ . The real ( $n$ ) part of CRI has been simulated using a Mie code for spherical particles varying  $n$  and  $k$  in the [1.3,2] and [0,0.2] respectively. The modelled value represents the value that minimises the root mean squared difference (RMSD) of Eq. 4. Only SMPS data has been taken into account.

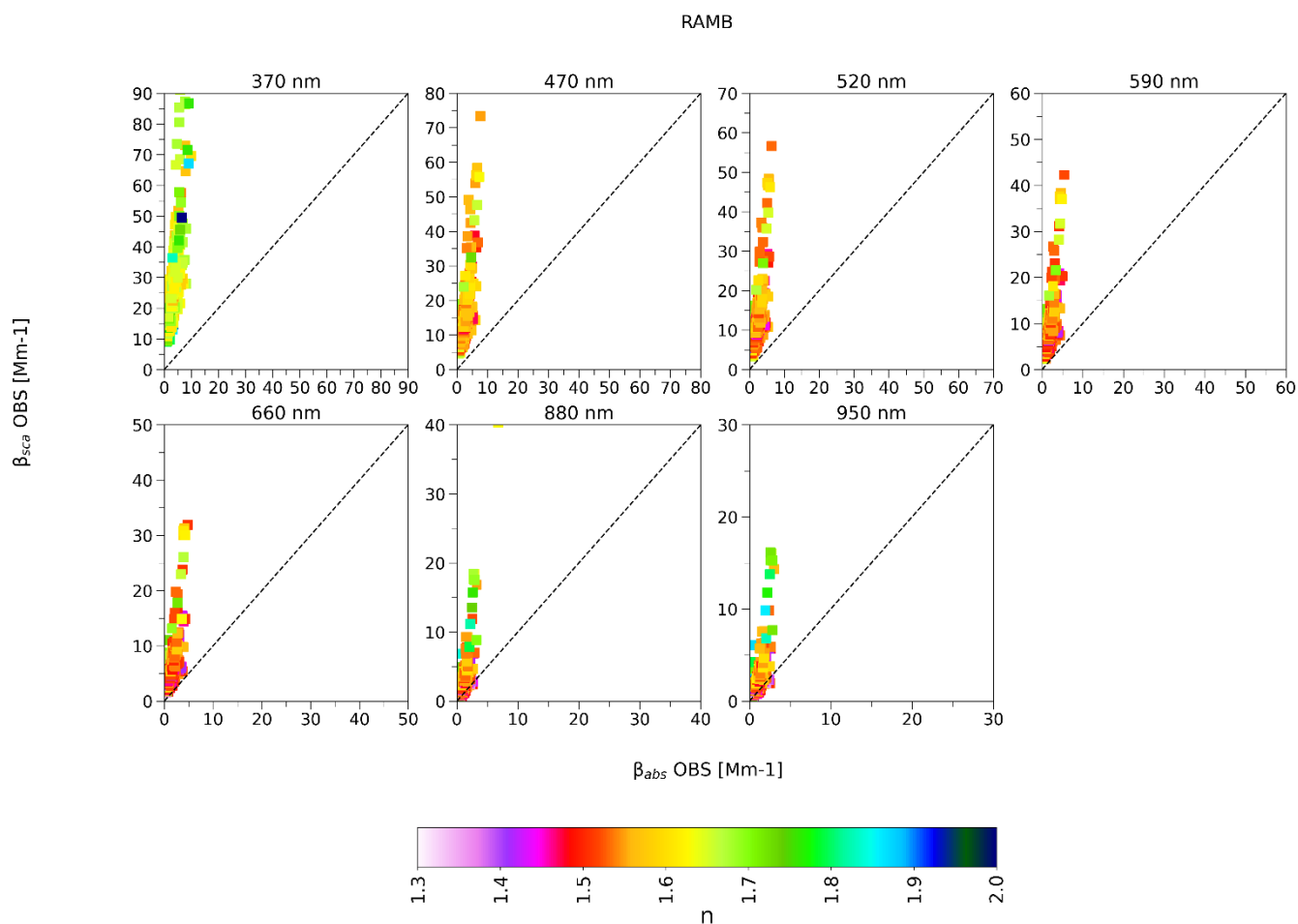
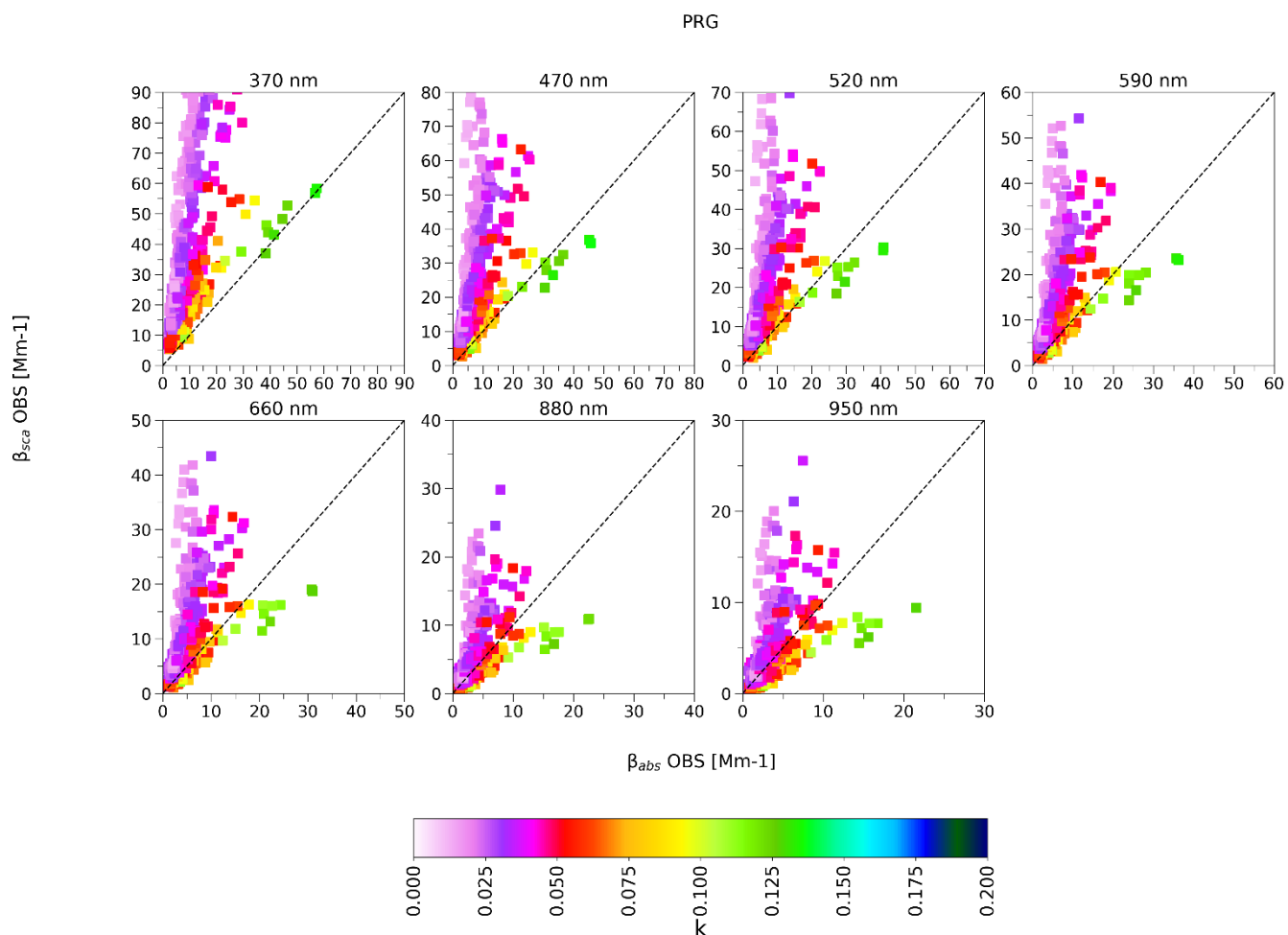


Figure S20: Scatter plot of hourly median observed scattering and absorption coefficient at seven different wavelengths and during the entire ACROSS campaign at the Rambouillet (forest site). The colours represent the simulated  $n$ . The real ( $n$ ) part of CRI has been simulated using a Mie code for spherical particles varying  $n$  and  $k$  in the [1.3,2] and [0,0.2] respectively. The modelled value represents the value that minimises the root mean squared difference (RMSD) of Eq. 4. Only SMPS data has been taken into account.



450 **Figure S21:** Scatter plot of hourly median observed scattering and absorption coefficient at seven different wavelengths and during the entire ACROSS campaign at the Paris Rive Gauche (urban site). The colours represent the simulated  $k$ . The imaginary ( $k$ ) part of CRI has been simulated using a Mie code for spherical particles varying  $n$  and  $k$  in the  $[1.3, 2]$  and  $[0, 0.2]$  respectively. The modelled value represents the value that minimises the root mean squared difference (RMSD) of Eq. 4. Only SMPS data has been taken into account.

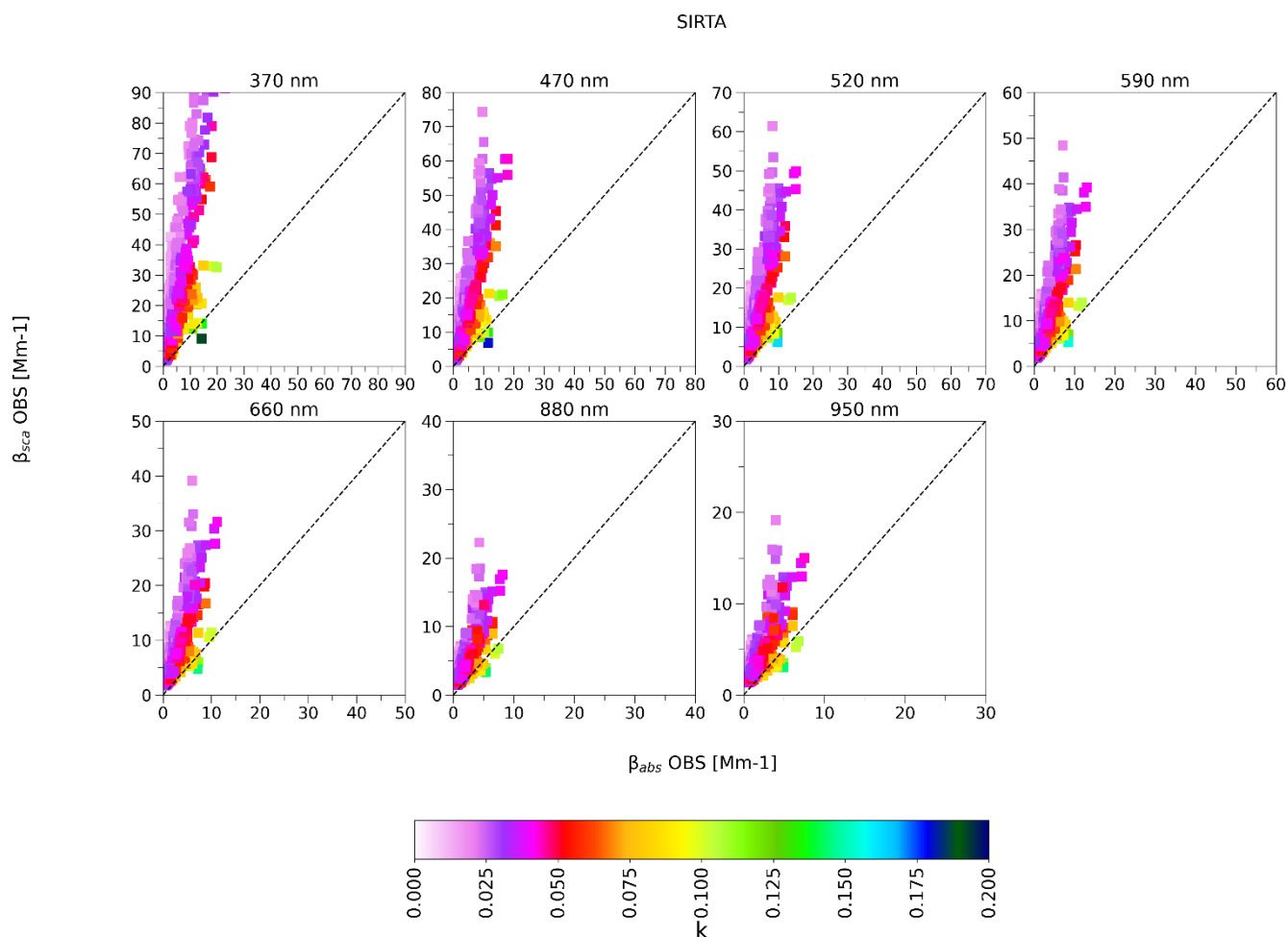
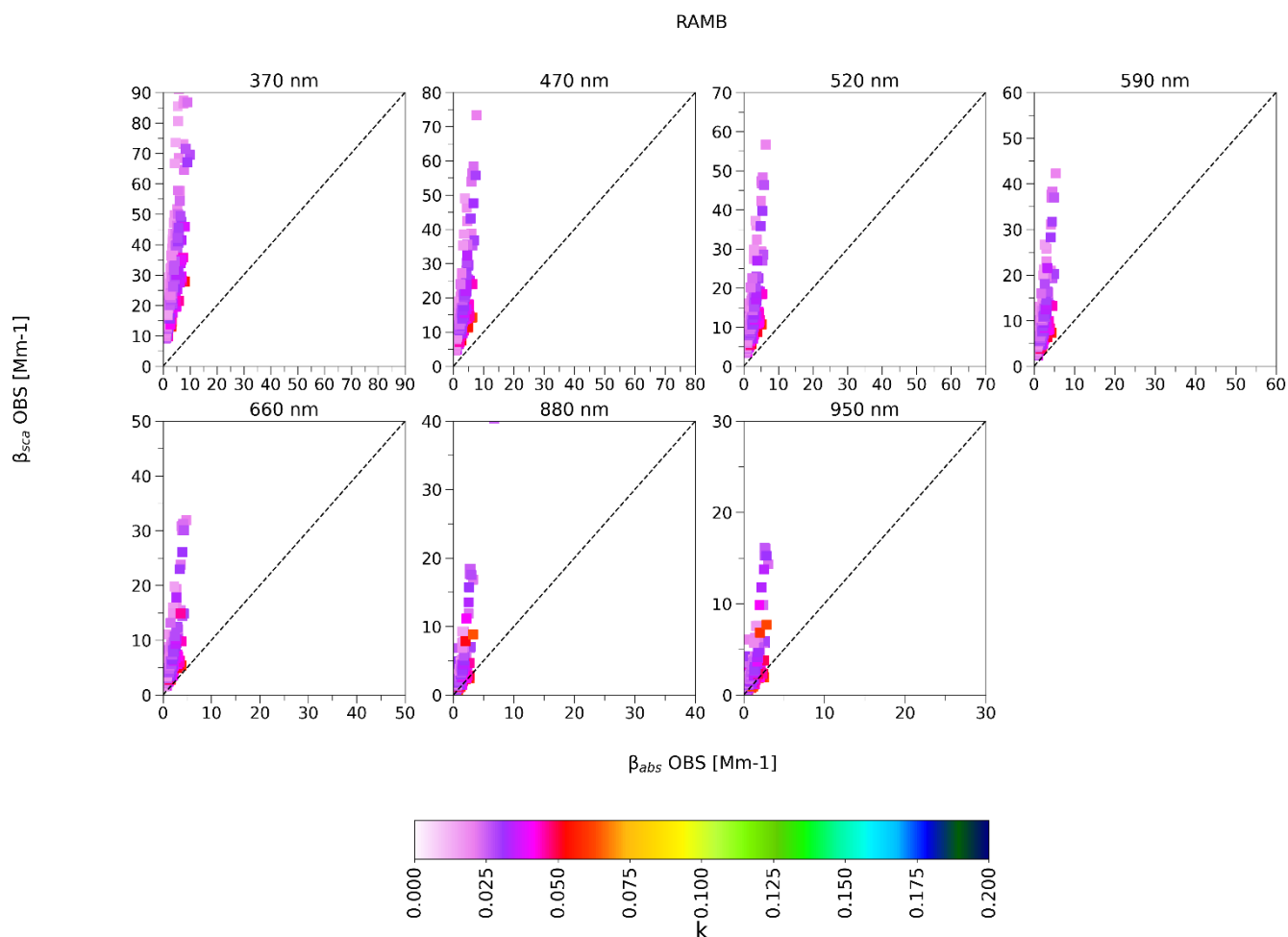
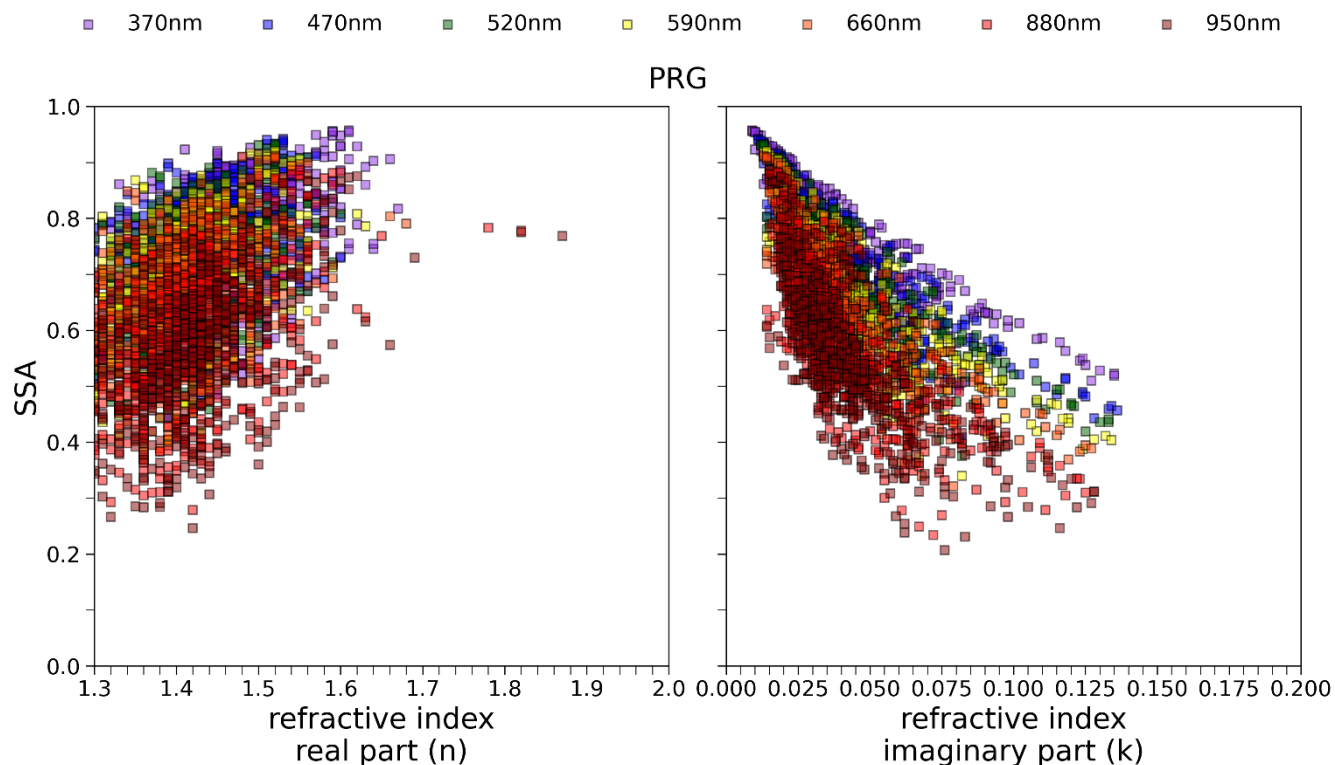


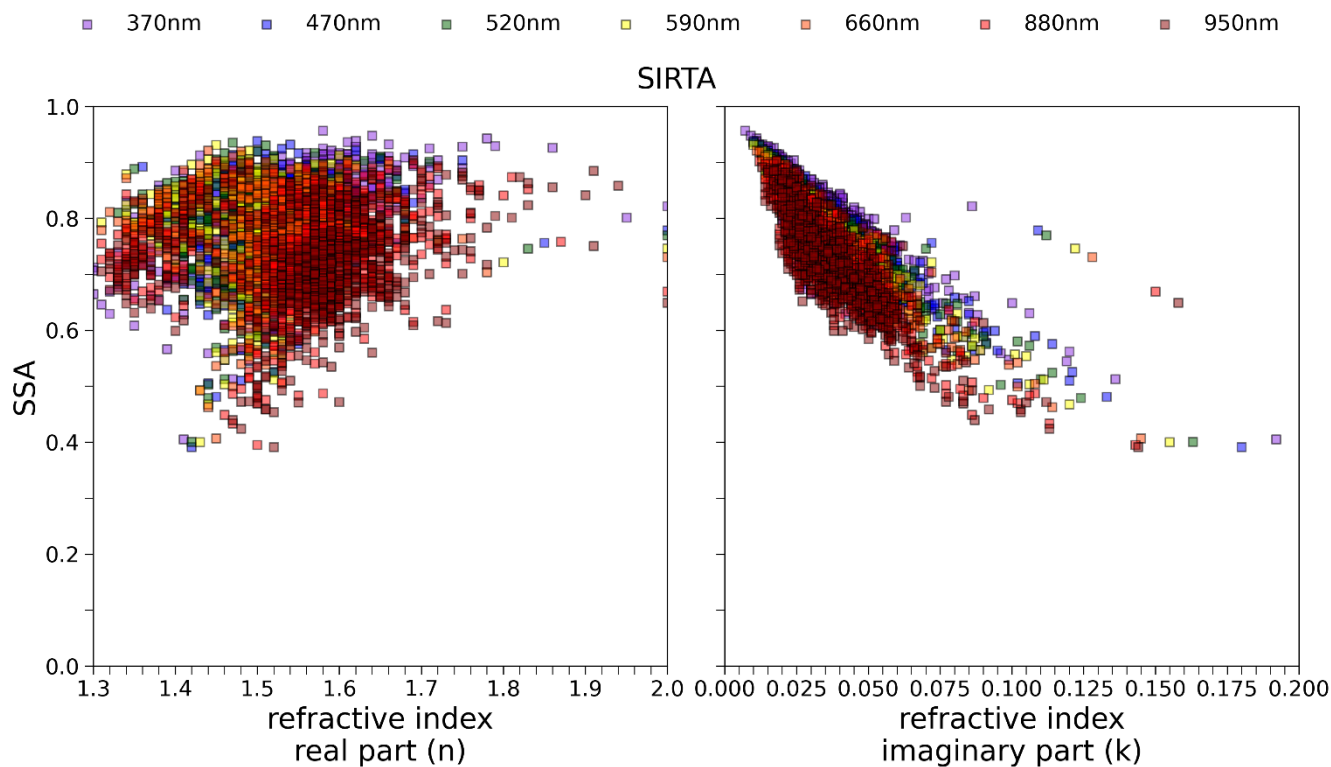
Figure S22: Scatter plot of hourly median observed scattering and absorption coefficient at seven different wavelengths and during the entire ACROSS campaign at the SIRTA (peri-urban site). The colours represent the simulated  $k$ . The imaginary ( $k$ ) part of CRI has been simulated using a Mie code for spherical particles varying  $n$  and  $k$  in the  $[1.3,2]$  and  $[0,0.2]$  respectively. The modelled value represents the value that minimises the root mean squared difference (RMSD) of Eq. 4. Only SMPS data has been taken into account.



**Figure S23: Scatter plot of hourly median observed scattering and absorption coefficient at seven different wavelengths and during the entire ACROSS campaign at the Rambouillet (forest site). The colours represent the simulated  $k$ . The imaginary ( $k$ ) part of CRI has been simulated using a Mie code for spherical particles varying  $n$  and  $k$  in the  $[1.3,2]$  and  $[0,0.2]$  respectively. The modelled value represents the value that minimises the root mean squared difference (RMSD) of Eq. 4. Only SMPS data has been taken into account.**



**Figure S24: Scatter plot of (left) hourly median observed single scattering albedo vs modelled real part and (right) hourly median observed single scattering albedo vs modelled imaginary part and of the refractive index at seven different wavelengths and during the entire ACROSS campaign at the Paris Rive Gauche (urban site). The colours represent the different wavelengths. The real ( $n$ ) and imaginary ( $k$ ) part of CRI have been simulated using a Mie code for spherical particles varying  $n$  and  $k$  in the  $[1.3, 2]$  and  $[0, 0.2]$  respectively. The modelled value represents the value that minimises the root mean squared difference (RMSD) of Eq. 4. Only SMPS data has been taken into account.**



490 **Figure S25: Scatter plot of (left) hourly median observed single scattering albedo vs modelled real part and (right) hourly median**  
**observed single scattering albedo vs modelled imaginary part and of the refractive index at seven different wavelengths and during**  
**the entire ACROSS campaign at the SIRTA (peri-urban site). The colours represent the different wavelengths. The real (n) and**  
**imaginary (k) part of CRI have been simulated using a Mie code for spherical particles varying n and k in the [1.3,2] and [0,0.2]**  
**respectively. The modelled value represents the value that minimises the root mean squared difference (RMSD) of Eq. 4. Only SMPS**  
495 **data has been taken into account.**

500

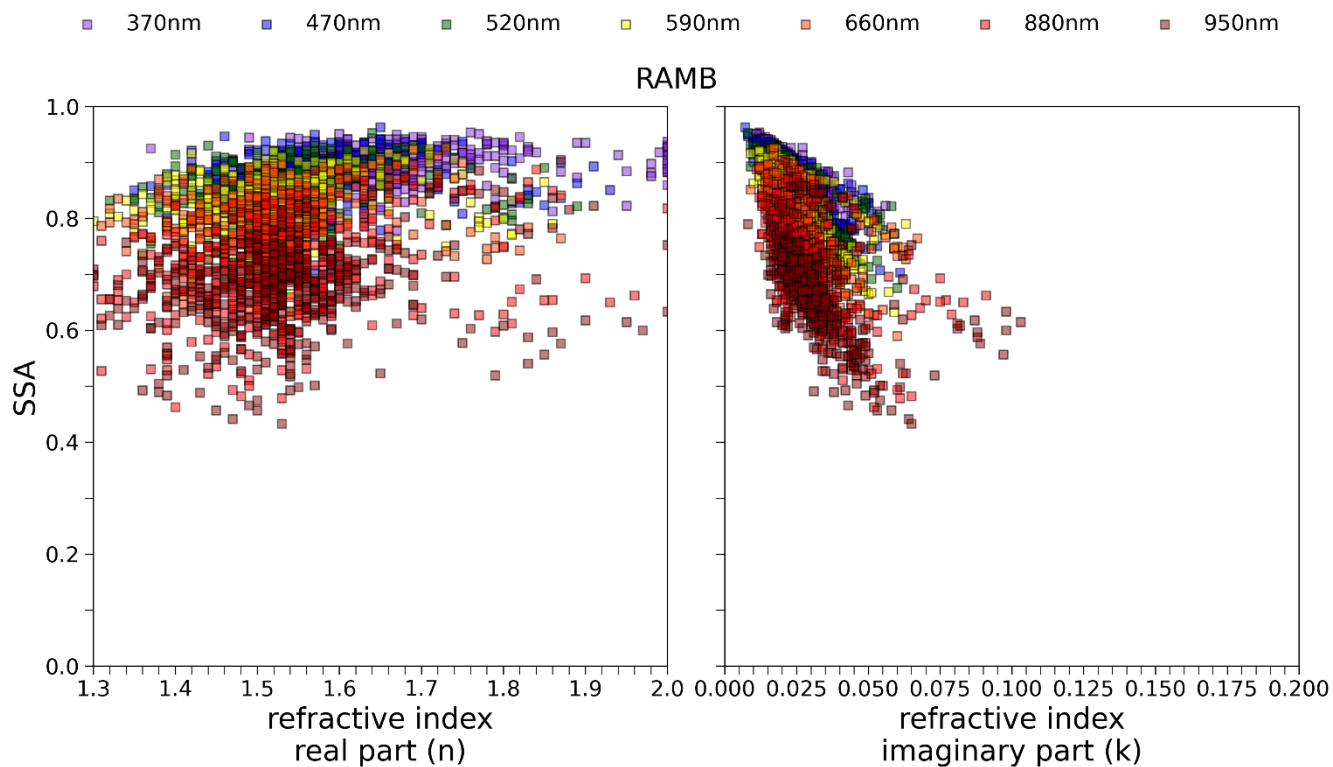


Figure S26: Scatter plot of (left) hourly median observed single scattering albedo vs modelled real part and (right) hourly median observed single scattering albedo vs modelled imaginary part and of the refractive index at seven different wavelengths and during the entire ACROSS campaign at the Rambouillet (forest site). The colours represent the different wavelengths. The real (n) and imaginary (k) part of CRI have been simulated using a Mie code for spherical particles varying n and k in the [1.3,2] and [0,0.2] respectively. The modelled value represents the value that minimises the root mean squared difference (RMSD) of Eq. 4. Only SMPS data has been taken into account.



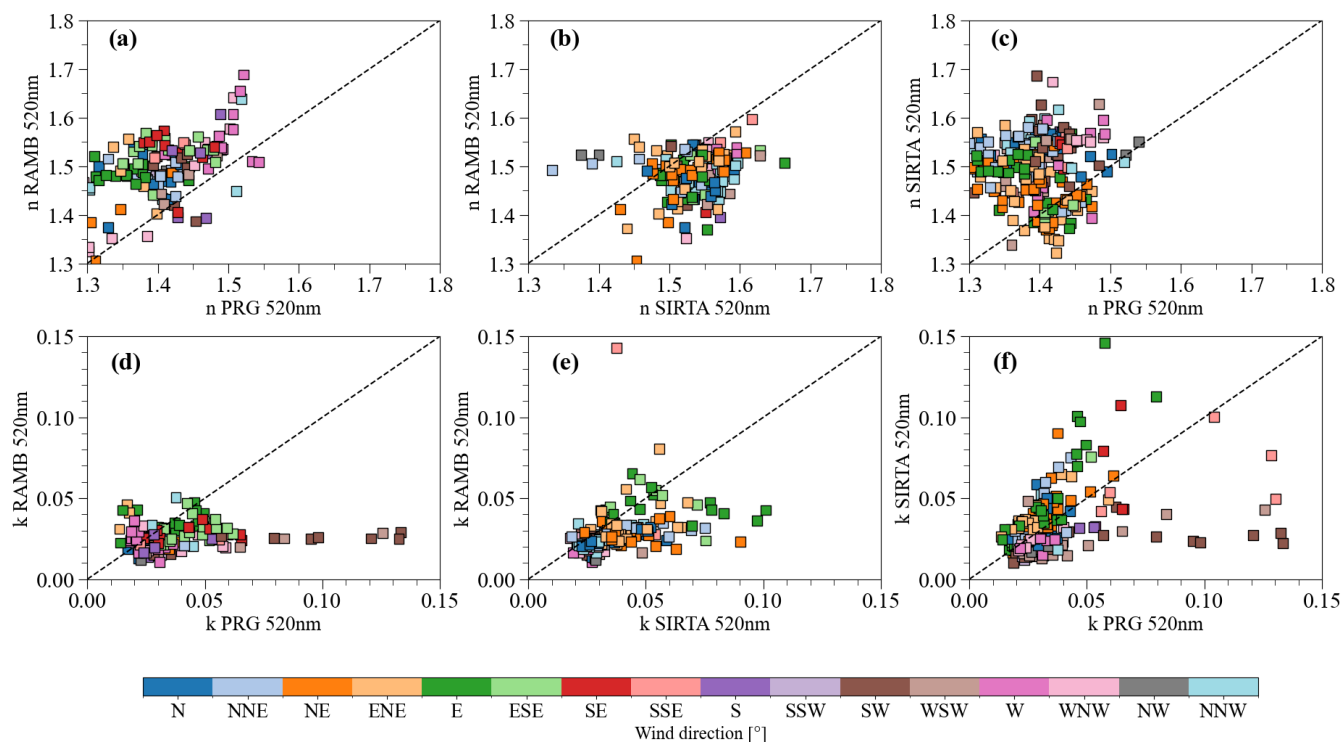
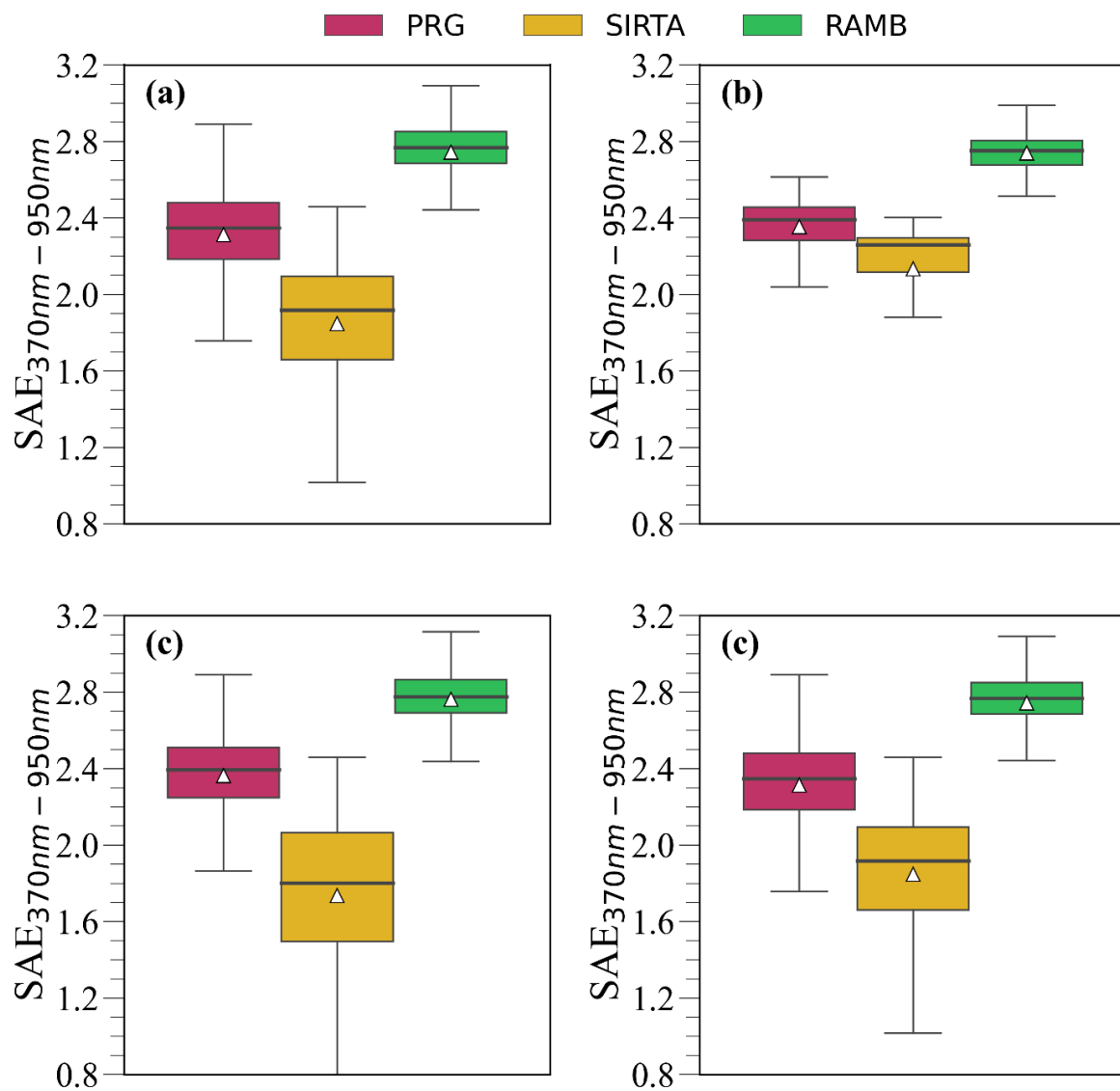


Figure S27: Scatter plot of real ( $n$ ) and imaginary ( $k$ ) part of the complex refractive index at 520 nm and at the three different sites: Paris Rive Gauche (PRG, urban), Sirta (peri-urban) and Rambouillet (RambForest, forest). Dashed line represents the 1:1 line. The CRI has been calculated as the mean of all simulations listed in Table 1. Colours represent the different wind directions.



535 **Figure S28:** Scattering Ångstrom exponent between 370 and 950 nm variability for (a) full period (b) first heatwave (c) clean period and (d) second heatwave. Black lines represent the boxplot median, while white triangles represent the boxplot mean.

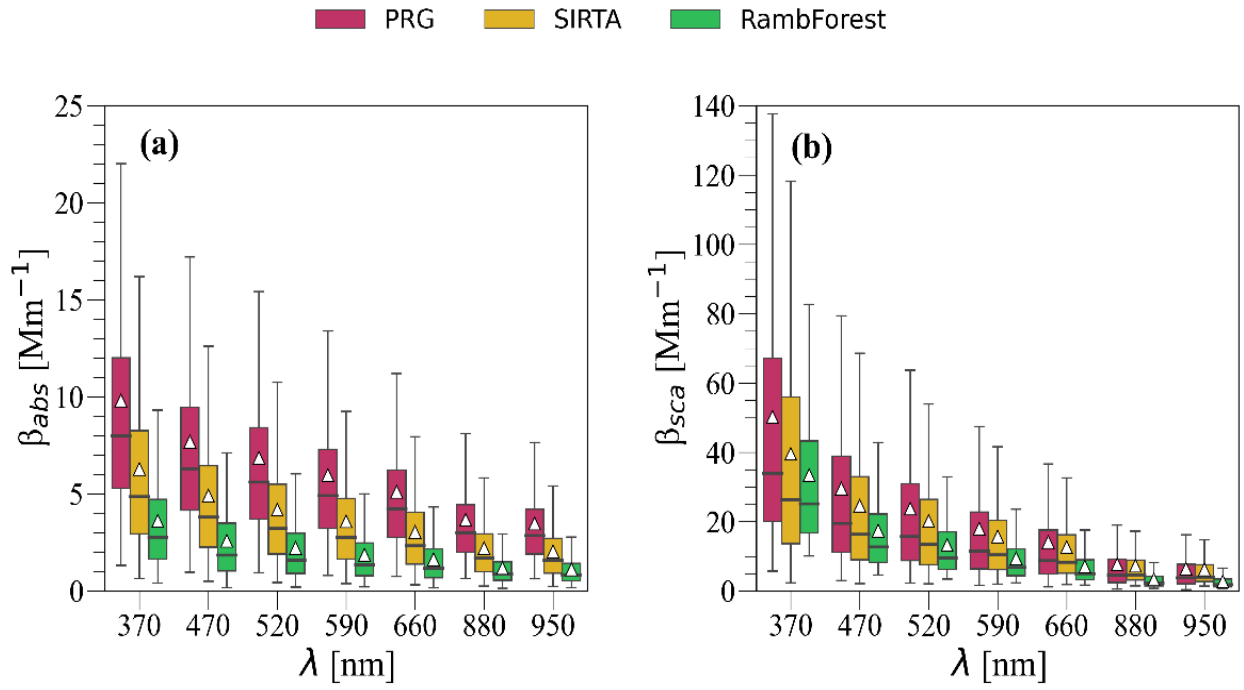


Figure S29: Wavelength dependence of a)  $\beta_{abs}$ , b)  $\beta_{sca}$  at Paris Rive Gauche (PRG,urban site), Sirta (peri-urban site) and Rambouillet (RambForest, forest site) for the 15 June–24 July 2022 period. The white triangles represent the mean values, while the median has been reported as the line crossing the boxplot.